PFC/JA-88-40

Power Balance Analysis of Ion Bernstein Wave Heating Experiments in the Alcator C Tokamak

John D. Moody and Miklos Porkolab

Plasma Fusion Center
Massachusetts Institute of Technology
Cambridge, MA 02139

December 1988

This paper is to be published in Physics of Fluids B.

This work was supported by the U. S. Department of Energy Contract No. DE-AC02-78ET51013. Reproduction, translation, publication, use and disposal, in whole or in part by or for the United States government is permitted.

Power Balance Analysis of Ion Bernstein Wave Heating Experiments in the Alcator C Tokamak

John D. Moody[a] and Miklos Porkolab

Plasma Fusion Center and Department of Physics,

Massachusetts Institute of Technology

Cambridge, MA 02139

Energy and particle transport processes in Alcator C [*Phys. Rev. Lett.*, **60**, 298, (1988)] discharges heated by directly launched ion Bernstein waves (IBW) are investigated using the ONETWO transport code [*Nucl. Fusion*, **26**, 329, (1986)]. The dependence of the observed ion heating rate ($\Delta T_H/P_{rf}$) on plasma density is shown to result mainly from the inherent ion energy confinement which is characteristic of these discharges in the Ohmic phase and not on IBW propagation and absorption characteristics. The inferred value of the Ohmic ion thermal conduction exhibits an increasing anomaly with increasing plasma density. At a plasma density of $\bar{n}_e \lesssim 1 \times 10^{20}\,\mathrm{m}^{-3}$, the inferred ion thermal conduction is nearly equal to the Chang–Hinton neoclassical prediction. However, at a plasma density of $\bar{n}_e \gtrsim 2 \times 10^{20}\,\mathrm{m}^{-3}$, the inferred ion thermal conduction increases to about 5–8 times the Chang–Hinton neoclassical value. This increasing anomaly, which may result from the ion temperature gradient driven instability, can essentially account for the observed ion heating rate behavior during IBW heating. The effect of edge turbulence on IBW propagation is modeled using a Monte Carlo direct sampling simulation. The result is mainly a radial broadening of the calculated power deposition profile with increasing plasma density.

---

a Current address: Department of Physics, University of California San Diego, La Jolla, California 92037

I. Introduction

Radio frequency power absorption via directly launched ion Bernstein waves (IBW) is presently being investigated as a means to heat laboratory plasmas to fusion ignition temperature [1] . Recent IBW experiments on the Alcator C tokamak at reactor relevant densities have been encouraging in several respects [2] : a large heating efficiency was observed ($\bar{n}_e \Delta T_H / P_{rf} \simeq 2$–$4.5 \times 10^{20}\,\mathrm{eV/kW\,m^{-3}}$) at $\bar{n}_e \simeq 1 \times 10^{20}\,\mathrm{m^{-3}}$, and improvements in the global particle and central impurity confinement time with respect to the Ohmic values were obtained; however, these favorable results showed a strong dependence on plasma parameters, especially the plasma density. For example, the high heating efficiency was strongly reduced above a line–averaged density $\bar{n}_e \gtrsim 1.5 \times 10^{20}\,\mathrm{m^{-3}}$, and the particle confinement was no longer improved with respect to the Ohmic value at $\bar{n}_e \geq 2.5 \times 10^{20}\,\mathrm{m^{-3}}$. In addition, the plasma impurity level showed a dependence on the plasma parameters. In this paper it is shown that the strong density dependence of the efficient ion heating is mainly due to the inherent ion energy confinement which is characteristic of these discharges in the Ohmic phase rather than a result of IBW propagation and absorption characteristics.

Earlier references [2, 3] suggested that the decrease in ion heating efficiency with increasing plasma density may have resulted from increased inaccessibility of the IBW power as the observed edge density turbulence increased with plasma density. This interpretation suggested that it was mainly the characteristics of the IBW (*i.e.* the short wavelength) which caused the wave power to strongly scatter from the turbulence leading to a decrease in the ion heating efficiency. More accurate energy and particle transport analyses, however, indicate that the ion heating rate decrease can be explained by the combined effects of wave scattering from the edge turbulence and by the decreasing ion energy confinement of these discharges with density. Using a Monte Carlo ray tracing simulation, the presence of edge turbulence is shown to cause a radial broadening of the rf power deposition profile with increasing plasma density. This, by itself, can only account for a fraction

of the ion heating rate decrease. Energy and particle transport modeling shows that the inferred value of the Ohmic ion thermal conduction, as compared to the Chang–Hinton neoclassical prediction, exhibits an increasing anomaly with increasing plasma density. This increasing anomaly, which is suggested to result from the presence of the ion temperature gradient driven instability [4, 5], can essentially account for the observed ion heating rate behavior during rf power injection in the Alcator C experiments. The measured ion temperature during rf power injection at both the $B_0 = 7.6\,\mathrm{T}$ and $9.3\,\mathrm{T}$ regimes can be explained by assuming that the ion thermal conduction remains nearly Ohmic–like. A slight difference observed between these two field regimes is suggested to result from different power deposition profiles and the characteristics of the ion temperature gradient driven instability.

The outline of this paper is as follows. Section II reviews the Alcator C IBW experimental results, focussing mainly on ion heating. In section III, the theory of IBW scattering from edge density fluctuations is described and the Monte Carlo ray tracing method which was used to model the effects of density turbulence on ion Bernstein wave propagation is presented. The calculated IBW power deposition profile is shown. This power deposition profile is then used as an ion power source in the ONETWO energy and particle transport code [6]. Section IV describes the energy and particle transport analysis of both Ohmic and rf heated discharges at $B_0 = 7.6\,\mathrm{T}$ and $B_0 = 9.3\,\mathrm{T}$. Section V reviews the results and presents the conclusions.

II. Alcator C IBW Experiments

IBW experiments were performed on the Alcator C tokamak to study wave excitation, propagation, absorption, and plasma heating. The following discussion will review some of the important features and results of the experiments which were presented in some detail in Refs. 2 and 3.

Ion Bernstein waves were launched from a stainless steel, center fed, T–shaped, movable loop antenna with the center conductor aligned along the direction of

the toroidal magnetic field and surrounded by a double layer, molybdenum coated Faraday shield. The experiments were conducted under the following conditions: rf frequency $f_0 = 183.6\,\mathrm{MHz}$; plasma minor radius (set by molybdenum limiters) $a =$ 0.115 m, 0.12 m, or 0.125 m ; major radius $R_0 = 0.64\,\mathrm{m}$; hydrogen majority plasma with a deuterium minority $0.1\% \lesssim n_D/(n_{H+D}) \lesssim 20\%$; toroidal magnetic field strength $4.8\,\mathrm{T} \leq B_0 \leq 11\,\mathrm{T}$; line–averaged electron density $0.6 \leq \bar{n}_e \leq 4 \times 10^{20}\,\mathrm{m}^{-3}$; $P_{\mathrm{rf}} \leq 180\,\mathrm{kW}$; plasma current $160\,\mathrm{kA} \leq I_p \leq 290\,\mathrm{kA}$; and $Z_{\mathrm{eff}} \sim 1$–4.

Measurement of the perpendicular wave–number spectrum of ion Bernstein waves using CO_2 laser scattering showed good agreement with the theoretical dispersion relationship [3] . The magnitude of the CO_2 scattered signal at $B_0 = 7.6\,\mathrm{T}$ also showed a nearly linear dependence on the rf power, further confirming that IBW power was coupled into the plasma. However, at $B_0 = 9.3\,\mathrm{T}$, little if any wave power was detected at the pump wave frequency in the plasma interior, indicating the possible occurrence of nonlinear processes near the plasma edge [7] .

Absorption of IBW power due to ion cyclotron damping is predicted by linear theory to occur where $\omega = n\omega_{cj}$ (n integer, j ion species). Nonlinear Landau damping, via self–interaction may occur where $\omega = \frac{1}{2}(2m+1)\omega_{cj}$ (m integer) and is predicted to dominate linear damping even in the presence of a minority species [8] . The details of IBW power absorption through either mechanism have been given in Ref. 8 and references therein. Calculated values of the nonlinear threshold power for a single ion species plasma at several central magnetic field values are in the range $P_{\mathrm{th}} \sim 10$–$40\,\mathrm{kW}$ and are given in Ref. 9. Another nonlinear process related to self–interaction and described by precisely the same physics is the parametric decay of an IBW into another IBW and an ion quasimode near the ion cyclotron frequency. This process has been described in Ref. 7 and details will be published elsewhere. The application of this process to IBW heating becomes important when the ion quasimode is resonant with a particular plasma ion species. For example, an IBW with $\omega_1/\Omega_{\mathrm{H}} = 1.6$ can decay into another IBW with $\omega_2/\Omega_{\mathrm{H}} = 1.1$ and an ion quasimode with $\omega_3/\Omega_{\mathrm{D}} = 1$ ($\omega_3/\Omega_{\mathrm{H}} = 0.5$). The deuterium species will absorb

the ion quasimode, while the daughter IBW is absorbed on hydrogen at a smaller value of the major radius where $\omega/\Omega_H \lesssim 1.1$.

Figure 1 shows the location of the hydrogen and deuterium cyclotron harmonics in the poloidal cross section for two magnetic fields. At $B_0 = 7.6\,\mathrm{T}$, power absorption is expected to occur either linearly on deuterium at the $\omega/\Omega_D = 3$ layer, located about 3.4 cm to the high field side of the plasma center ($x/a = -0.3$ where $x = R - R_0$), via ion cyclotron damping, or nonlinearly on hydrogen at the $\omega/\Omega_H = 1.5$ layer (same location) via IBW self–interaction, or nonlinearly on deuterium near the $\omega/\Omega_H \simeq 1.6$ layer via IBW decay. At 9.3 T, rf power absorption in the plasma interior is expected to occur nonlinearly on deuterium at the $\omega/\Omega_D = 2.5$ layer located about 4.5 cm to the high field side of the plasma center, via self–interaction.

Central ion temperature increases ($\Delta T_i/T_i \gtrsim 0.1$) of the hydrogen majority component were observed on Alcator C during rf power injection for magnetic fields in the range $4.8\,\mathrm{T} \leq B_0 \leq 11\,\mathrm{T}$. Although the greatest ion temperature increase was observed at $B_0 = 9.3\,\mathrm{T}$, heating occurred over a broad range of magnetic fields ($2.4 \geq \omega/\Omega_{H(0)} \geq 1.1$) and was not strongly dependent on having a particular ion cyclotron resonance located near the plasma center. The majority of heating studies were conducted in discharges at $B_0 \simeq 7.6\,\mathrm{T}$, 5.1 T, and 9.3 T, having an axial safety factor value $q(0) \lesssim 1$. Due to limited power injection at $B = 5.1\,\mathrm{T}$, the ion temperature increase at this field regime was comparable to the uncertainty in the ion temperature measurement. Therefore, only data at the $B_0 = 7.6\,\mathrm{T}$ and $B_0 = 9.3\,\mathrm{T}$ regimes is analyzed.

Power attenuation of the IBW in the Alcator C plasma was observed using CO_2 laser scattering techniques across the $\omega = 1.5\,\Omega_H$ layer at the 7.6 T regime [3]. This may be an indication of linear power absorption on the deuterium or nonlinear absorption on the hydrogen. A peak in both the radiation resistance and the scattered laser power was observed at a central magnetic field of 7.6 T; this corresponds to $\omega/\Omega_H \sim 1.95$ just behind (to the low field side of) the antenna. Theoretically,

it is expected that efficient direct launching of IBW power should occur when the $\omega/\Omega_H \sim 1.99$ layer is placed just behind the antenna [10] . A nearly field independent background loading of about $1\,\Omega$ was observed on either side of the peak. This background may be caused by dissipation due to anomalous processes which are not well understood.

A strong decrease in the ion heating rate was observed for target plasma densities $\bar{n}_e \gtrsim 1.1 \times 10^{20}\,\mathrm{m}^{-3}$, and as shown in Fig. 2 , significant increases in the ion temperature were not seen for target densities $\bar{n}_e > 2.5 \times 10^{20}\,\mathrm{m}^{-3}$ and at rf powers $P_{rf} \lesssim 100\,\mathrm{kW}$ ($4.8\,\mathrm{T} < B_0 < 11\,\mathrm{T}$). The increases in T_i for $\bar{n}_e > 2.5 \times 10^{20}\,\mathrm{m}^{-3}$ are within the experimental error of $\Delta T_i \simeq 0$. In particular, at high densities it was difficult to inject more than $\sim 100\,\mathrm{kW}$ from the antenna (antenna power density $P/A \sim 1\,\mathrm{kW/cm^2}$). The large scatter in the data in Fig. 2 appears on a day–to–day basis whereas the error bar represents typical scatter within a single day. The large scatter is thought to result from day–to–day variations in the plasma edge conditions which affect the antenna–plasma coupling. It is pointed out that the envelope of the data in Fig. 2 is what exhibits the maximum achievable ion heating rate; this envelope exhibits a trend toward decreasing ion heating rate with increasing density. There is a lack of data near $\bar{n}_e \simeq 2 \times 10^{20}\,\mathrm{m}^{-3}$ which may account for the apparent increase in heating rate above this density. The envelope also seems to show a decrease in heating rate below $\bar{n}_e \simeq 0.75 \times 10^{20}\,\mathrm{m}^{-3}$. Due to lack of sufficient data, transport processes have not been studied in this low density regime where electron transport processes dominate.

Several mechanisms which have a density dependent effect on the ion heating rate have been considered to explain the ion heating rate decrease. For example, wave power attenuation due to edge collisions becomes stronger as the density is increased. Theoretical estimates of collisional damping [11] indicate that edge absorption is negligible even for an edge density and temperature of $n_e(r = a) \simeq 1 \times 10^{20}\ \mathrm{m}^{-3}$, $T_e \sim T_i \sim 50$ eV, characteristic of high density discharges. The nonlinear power threshold, which increases linearly with increasing plasma density,

may account for some of the decrease in the heating rate. However, the decrease is more sudden than expected and linear damping of IBW power on the deuterium minority (at $B_0 = 7.6\,\mathrm{T}$) should still occur even at high density. Another effect which may partly account for the decrease in the heating rate is the saturation of the neo–Alcator energy confinement scaling which is proportional to density at $\bar{n}_e \sim 1.5 \times 10^{20}\,\mathrm{m}^{-3}$. This saturation is caused by both increased coupling between the electrons and ions, and an increasing anomaly in the ion thermal diffusivity when compared to the Chang–Hinton neoclassical prediction. Thus, the ion energy confinement time degrades as the density is increased and this contributes to the observed decrease in the ion heating rate.

CO_2 scattering results suggest that the decrease in the ion heating rate may partially be attributed to inaccessibility of the IBW to the plasma center due to scattering from low–frequency edge density fluctuations ($\tilde{n}_e/n_e \gtrsim 0.3$ at $r/a \simeq 0.9$) as the target density is increased. The quantity $\tilde{n}_e$ indicates the absolute amplitude of the low–frequency density fluctuation. To investigate the possibility that density fluctuations may impede the IBW power from propagating into the plasma interior, the CO_2 scattering diagnostic was reconfigured to observe fluctuations in the edge plasma [3] . Although the absolute magnitude of $\tilde{n}_e/n_e$ could not be determined with accuracy in these measurements, based on earlier measurements it was estimated to be in the range of 0.1–0.4 at a density of $\bar{n}_e \gtrsim 2 \times 10^{20}\,\mathrm{m}^{-3}$ [12] . The strong correlation which is observed between the scattered power from ion Bernstein waves in the plasma center and the scattered power from low–frequency edge density fluctuations suggests that edge turbulent scattering may affect the wave accessibility to the plasma center. In the next section we investigate the effect of low–frequency density fluctuations on IBW propagation.

III. IBW Scattering from Density Fluctuations

A. Observation

Figure 3 shows that the edge density fluctuation amplitude exhibits a minimum at a line–averaged density of $\bar{n}_e \simeq 1.1 \times 10^{20}\,\mathrm{m}^{-3}$ and increases for both higher and lower densities. This behavior is inversely correlated with the amplitude of the scattered signal from IBW power near the plasma center and with the hydrogen ion heating rate $\Delta T_i/P_{rf}$ (Fig. 2). Both the ion heating rate and the scattered signal from IBW power show a decrease in their value for densities above $\bar{n}_e \gtrsim 1.1 \times 10^{20}\,\mathrm{m}^{-3}$.

B. Expected Behavior of $\hat{n}_e$

The scattered CO_2 laser power is proportional to the integral of $\tilde{n}_e^2$ over the scattering volume which consists of the region defined by the intersection of the CO_2 laser beam and the plasma. It is necessary to determine the expected behavior of $\tilde{n}_e^2$ in the absence of turbulent fluctuations in order to tell how strongly the data in Fig. 3 (a) deviates from this. The deviation is then an indication of the effect of turbulence on IBW propagation.

The normalized electron density fluctuation amplitude $\hat{n}_e$ can be written in terms of the IBW electric field amplitude E_x and the dielectric tensor elements: [3]

$$\hat{n}_e \equiv \frac{\tilde{n}_e}{n_e} = i\frac{e}{m_e c\omega}\left[\frac{\omega^2}{\omega_e^2} - i\frac{\omega}{\omega_e}\frac{K_{xy}}{K_{xx} - n_\parallel^2 - n_\perp^2} - \frac{n_\parallel^2}{n_\perp^2 - K_{zz}}\right] n_\perp E_x \qquad (1)$$

where $\omega_e = |\Omega_e|$. The electric field amplitude $|E_x|$ is related to the wave power P as

$$P = \frac{\omega}{8\pi}\frac{\partial \epsilon}{\partial k_\perp}|E_x|^2 S \qquad (2)$$

where S is the wave surface area. The precise behavior of $\hat{n}_e$ with density is complicated since it depends on the dominant term(s) in Eq. (1) and on the electric field. To partly simplify the analysis of Eq. (1) it is assumed that the antenna is

operating under good coupling conditions, *i.e.*, the total power coupled into the IBW is essentially independent of density. In this case, the value of P in Eq. (2) is density independent. In addition (for the experimental range of densities), the perpendicular wave vector $k_\perp$ is independent of density. The dielectric constant, ϵ is proportional to the density for the range of densities considered here, thus $\partial\epsilon/\partial k_\perp$ is also proportional to the density. The wave surface area S depends on the extent to which the ion Bernstein waves have spread by the time they reach the scattering volume. The scattering volume extends over the length of the plasma in the poloidal cross section, therefore wave spreading in the poloidal cross section does not affect the integrated scattered power. Wave spreading in the toroidal direction does, however, affect the integrated scattered power since the scattering volume has finite toroidal extent. Toroidal wave spreading is primarily determined by the value of $n_\parallel$ and less importantly by the spatial profiles of the plasma parameters. For large $n_\parallel$ (> 1), the toroidal wave spreading is approximately independent of density provided the spatial profile of the plasma density and temperature is only weakly dependent on plasma density. Experimentally, a weak density dependence of the temperature and density profiles is observed at the 7.6 T and 9.3 T magnetic field regimes. The details of these profiles and their associated uncertainty is given in section IV B and IV H. In addition, numerical modeling shows that the $n_\parallel$ power spectrum remains relatively constant over the density range considered. It can therefore be concluded that S is essentially independent of density. It is pointed out that the CO_2 laser scattering system can only observe waves with wave vector $\mathbf{k}$ perpendicular to the incident laser $\mathbf{k_0}$; it is possible that the fraction of observable wave power may change with density. This is difficult to determine, but based on numerical simulations of IBW ray trajectories, the effect is not expected to be important. It can be concluded at this point from Eq. (2) that for constant P, $|E_s|$ is approximately proportional to $n_e^{-1/2}$.

The dominant term inside the square brackets in Eq. (1) for the densities considered here is primarily dependent on the value of $n_\parallel$, with a weaker dependence

on the plasma density. For small $n_\parallel$ ($<< 1$), the second term, which increases approximately linearly with density, determines the overall behavior of $\hat{n}_e$. For example, when $n_\parallel = 0.1$ the value of $\tilde{n}_e^2$ increases by a factor of 20 as the density increases from $\bar{n}_e = 1 \times 10^{20}\,\mathrm{m}^{-3}$ to $4 \times 10^{20}\,\mathrm{m}^{-3}$. If the CO_2 laser scatters off IBW with small $n_\parallel$, the data in Fig. 3 (a) indicates that the observed IBW power is strongly reduced with increasing density compared to the expected value. For large values of $n_\parallel$ (> 1), the third term, which decreases with density, determines the behavior of $\hat{n}_e$. The $n_\parallel$ power spectrum expected to be in the plasma is peaked at $n_\parallel = \pm 5$. This spectrum is calculated using the theory described in Ref. 10 and the result is shown in Ref. 13. The dashed line in Fig. 3 (a) shows the overall expected value of P_{scat} (normalized to the observed value of P_{scat} at $\bar{n}_e = 1.1 \times 10^{20}\,\mathrm{m}^{-3}$) for $n_\parallel = 5$. The decrease in the expected value of P_{scat} with density is not quite as strong as the measured decrease. If the CO_2 laser scatters off IBW with large $n_\parallel$, the data at high density indicates that the IBW power is only weakly reduced from what is expected. The CO_2 laser scattering system preferentially observes IBW power with small $n_\parallel$ ($<< 1$) since most of the wave power which enters the scattering volume must propagate nearly perpendicularly to the antenna surface. Therefore, it is most likely that the data shown in Fig. 3 (a) is dominated by laser power scattered from IBW with small $n_\parallel$. This indicates that the IBW power entering the CO_2 laser scattering region is reduced with increasing plasma density.

C. Theory of Ion Bernstein Wave Scattering

In order to quantitatively investigate the effects of edge density turbulence on IBW propagation, a ray tracing model was developed and used to solve the wave kinetic equation describing IBW scattering from density turbulence. The method used to solve the kinetic equation is described as a Monte Carlo direct sampling simulation [14] . This type of method has been used previously by Bonoli to model the turbulent scattering of lower hybrid waves [15] . This section discusses the details of the scattering process and presents the method used for modeling the effect of

plasma turbulence on IBW propagation in the Alcator C tokamak. The results of this model also will be presented and discussed.

Ono has previously described the theory of wave–wave interaction between ion Bernstein waves and density turbulence [16] . Since the measured frequency of the density fluctuations is small compared to the ion cyclotron frequency, the frequency shift in the scattered IBW can be neglected. Also, the parallel wave number can be considered to be conserved since $k_{\|}$ of the IBW is typically much larger than the average $k_{\|}$ of the fluctuation. The main effect, therefore, of the scattering can be well represented simply by a rotation of the IBW perpendicular wave vector $\mathbf{k}_{\perp}$ through an angle β. The scattering probability is calculated by using the random phase approximation [17] .

It has been found experimentally that the density fluctuation wave number spectrum is well approximated by the expression [18]

$$S_e(\xi) = \frac{1}{\pi \xi_0} |\hat{n}_e|^2 \exp\left[-\frac{\xi^2}{\xi_0^2}\right] \tag{3}$$

where ξ_0 is the root–mean–square (rms) value of the fluctuation wave number spectrum. Defining L_s as the perpendicular distance traveled by the IBW by the time it decays to $\sim 37\%$ $(1/e)$ of its initial amplitude, for fixed $\xi_0 \rho_i$, Ono finds [16]

$$L_s \propto \sqrt{T_i}/(B_0 |\hat{n}_e|^2) \tag{4}$$

which is independent of the plasma density.

D. Numerical Procedure

The numerical study of the scattering process proceeds as follows. The Brambilla coupling model is first used to obtain the k_y and k_z antenna power spectrum [10] . This spectrum is then divided into 106 regions, each with a corresponding power, k_y (k_θ), and k_z (k_ϕ) value. A toroidal ray tracing code is next used to advance a ray (representing one region of the power spectrum) in time by Δt [13] . The probability

of a scattering event occurring in time Δt during which the IBW perpendicular wave vector is rotated through any angle $-\pi \leq \beta \leq \pi$, is given by the expression [15]

$$P_{\text{total}} = \Delta t \int_{-\pi}^{\pi} P(\beta, t)\, d\beta. \tag{5}$$

The value of Δt is selected so that $P_{\text{total}} << 1$. This prohibits multiple scattering events occurring during the time interval Δt. A random number n_p, with uniform distribution between 0 and 1 is generated. If $P_{\text{total}} \geq n_p$ the ray is scattered, otherwise the ray is advanced another unit in time by Δt, and P_{total} is again calculated and compared with a new random value of n_p. If the ray is to be scattered, a random angle β is generated with the distribution

$$G(\beta) = \frac{P(\beta)}{\int_{-\pi}^{\pi} P(\beta)\, d\beta}. \tag{6}$$

This is done numerically by generating a random number n_β with uniform distribution between $-\pi$ and π. The scattering probability $P(n_\beta)$ is calculated for this number. A second random number n_p is then generated with a uniform distribution between 0 and 1. If $P(n_\beta) \leq n_p$ the random number n_β is accepted as the scattering angle β. If $P(n_\beta) > n_p$, this process is repeated again with two new random numbers n_β and n_p until a random number n_β is selected. Once a scattering angle is determined, the wave vector $k_\perp$ is rotated through this angle. The ray tracing calculation is now resumed, the ray is advanced in time by Δt and the probability of scattering is once again calculated.

E. Power Deposition

Linear power deposition is calculated using the power transport equation [19]. This equation is included in the set of ray equations and is numerically integrated along the ray as the ray is traced. The difference in ray power from one time step to the next is equal to the power deposited locally in the plasma in that time step. The radial power deposition profile is calculated numerically by first dividing the minor

radius into 50 equal divisions or bins. Each bin represents a *radial shell* centered around the magnetic axis. As each ray is traced, the power absorbed between time steps is accumulated in the radial bin corresponding to the present location of the ray. This process is repeated for each ray. Once all of the rays are traced, the power collected in each bin is normalized to the total launched power. The result is the radial power deposition profile.

The random selection of scattering angles and the random decision of whether to scatter the ray makes this particular method a Monte Carlo direct sampling simulation. In principle, as the number of rays traced becomes infinite, the power deposition profile converges to the solution of the wave kinetic equation. Since this is a statistical method of solving the kinetic equation and the number of rays traced is finite (106 rays), the error in the resulting power deposition is proportional to $N^{-1/2}$ where N is the total number of rays traced. For the cases modeled here the error is about 10%.

Finally, it is useful to verify that the kinetic equation is valid throughout the plasma region of interest. This is true provided that the coherence length of the IBW, l_{IBW} is greater than the correlation length of the fluctuations $\sim 1/\xi_0$. If this is true, coherent phase effects between individual Fourier turbulent modes can be neglected. This condition is satisfied within a wide margin throughout the plasma.

F. Numerical Results

Monte Carlo solutions to the kinetic equation were obtained numerically for the following plasma parameters: $0.5 \times 10^{20}\,\mathrm{m}^{-3} \leq \bar{n}_e \leq 2 \times 10^{20}\,\mathrm{m}^{-3}$, $T_i = 900\,\mathrm{eV}$, $T_e = 1800\,\mathrm{eV}$, $I_p = 250\,\mathrm{kA}$, $B_0 = 7.6\,\mathrm{T}$, $n_D/n_e = 0.1$, and $0 \leq \hat{n}_e \leq 0.5$. The density and temperature profiles were parameterized as

$$n(\rho) = n_{\mathrm{edge}} + (n_0 - n_{\mathrm{edge}}) \left[1 - \left(\frac{\rho}{a}\right)^2\right]^{\alpha_n} \tag{7}$$

$$T(\rho) = T_{\mathrm{edge}} + (T_0 - T_{\mathrm{edge}}) \left[1 - \left(\frac{\rho}{a}\right)^2\right]^{\alpha_T} \tag{8}$$

where $\alpha_n = 1.2$, $\alpha_T = 2$, $n_{edge} = 7 \times 10^{18}\,m^{-3}$, and $T_{edge} = 40\,eV$. The power deposition profile was calculated as a function of plasma density and scattering amplitude. The radial density fluctuation profile was modeled as a Gaussian with a peak at $\rho/a = 0.95$ and a radial full width at half maximum of 2 cm. Although accurate measurements of the turbulent radial profile were not available in the IBW experiments, these profile characteristics were inferred from earlier measurements [12]. Several of the scattering experiments discussed in Ref. 12 were performed on Alcator C in discharges with minor radii $7\,cm \leq a \leq 16.5\,cm$, magnetic field $B \sim 7\,T$, and density $1 \times 10^{20}\,m^{-3} \leq \bar{n}_e \leq 10 \times 10^{20}\,m^{-3}$. The similarity between these types of discharges and the discharges used in the IBW experiments suggest that the fluctuation behavior in Ref. 12 is a good description of the fluctuations in these discharges. The maximum amplitude of $\hat{n}_e$ is estimated from Ref. 12 to be in the range $0.1 - 0.4$ for $\bar{n}_e = 2 \times 10^{20}\,m^{-3}$.

Linear power absorption was calculated for electron Landau damping and ion cyclotron damping on the deuterium species. Nonlinear damping mechanisms were not included in this calculation. Once the power in a single ray was attenuated to less than 0.1% of the initial power, that ray was assumed completely absorbed and another ray was then traced. Each ray was individually traced for a time t_0 which was long enough so that unimpeded by fluctuations and undamped, a ray could cross the poloidal cross section slightly more than once. Some rays which underwent many scattering events still had a fraction of their initial power undamped after time t_0. This power was discarded and not included in the total radial power deposition. As a result, the total absorbed power was always between 80% and 100% of the total launched power. In principle, tracing the rays for a longer time would cause the remaining power to be absorbed in a profile similar to the profile of the power already absorbed and wouldn't change the main conclusions of this study.

Rays which scattered into radial locations $\rho > \rho_0$, where ρ_0 is the radial starting position of the ray, were assumed to be scattered out of the plasma and absorbed at the plasma edge. Figure 4 shows the effect of increasing the scattering

amplitude on IBW rays at a plasma central density of $1.5\times10^{20}\,\mathrm{m}^{-3}$. The histograms indicate the absorbed power density normalized to unity. [20] The large power density at $\rho \sim 2$–$3\,\mathrm{cm}$ is due to absorption at the $\omega/\Omega_D = 3$ layer located at $x = -3.4\,\mathrm{cm}$. The width of the absorption peak is characteristic of the spread in $k_\parallel$ of the rays. The remainder of the absorption results from electron Landau damping and exhibits a minimum near $x \sim 7\,\mathrm{cm}$. This is the location where rays with the majority of the power encounter a toroidal bounce point ($k_\parallel \simeq 0$) and there is very little electron Landau damping here.

As the scattering amplitude is increased, the power reaching the plasma center ($\rho/a \leq 0.5$) is noticeably decreased. This is caused (in this model) by an increasing fraction of power which is both deposited at the plasma edge as well as absorbed on the electrons via electron Landau damping. The power deposited at the plasma edge results from rays which are scattered out of the plasma. The reason for the increased electron Landau damping is two–fold. First, the scattered rays may undergo multiple passes through the electron Landau damping region as the direction of their ray trajectory is changed at each scattering event. Second, the value of $k_\parallel$, although not changed by a scattering event, can increase due to toroidal effects as the ray trajectory is altered in a scattering event. M. Brambilla suggests that IBW ray tracing, in general, overestimates the power which is electron Landau damped [21] . This can be shown by comparing a ray tracing calculation of the rf power deposition with a full wave calculation. Considering this, it is likely that the scattered rays do not undergo increased damping on the electrons but eventually find their way to the $\omega/\Omega_D = 3$ layer where they damp on the ions (deuterium ions in this model). The primary effect of scattering in this case is then to spread the power reaching the absorption layer over a wider radial region. This effect can be approximated from the numerical results by simply assuming that the calculated radial power density (shown in Fig. 4 and 5) represents the power deposited into the ions. The total power deposited in the plasma region where $\rho/a \leq 0.5$ is then used as a means of estimating the effect of the wave scattering on IBW propagation.

A scattering amplitude of about 30% is sufficient to prevent a large fraction of the IBW power from penetrating to the plasma center. Figure 5 shows the effect of increasing the fluctuation amplitude on IBW power deposition at a higher central density. The effect is essentially the same; a 30% value of $\hat{n}_e$ is sufficient to prevent much of the power from reaching the plasma center.

Figure 6 (a) shows the predicted fraction of power which propagates into the inner 1/2 of the plasma as a function of density; the measured scattering amplitude is shown for comparison in Fig. 6 (b). The curve in Fig. 6 (a) is obtained as follows. An upper bound of 40% is set for $\hat{n}_e$ which corresponds to the value of 10 in arbitrary units for $\hat{n}_e^2$. This upper bound is selected according to the measurements in Ref. 12. Values of $\hat{n}_e$ corresponding to each density are obtained from the data in Fig. 6 (b). Using these values of $\hat{n}_e$, the amount of power reaching the inner 1/2 of the plasma is calculated by solving the kinetic equation using the Monte Carlo method already outlined. The power reaching the plasma region where $\rho/a \leq 0.5$ decreases by about a factor of four when the density increases from $\bar{n}_e = 1 \times 10^{20}\,\mathrm{m}^{-3}$ to $3 \times 10^{20}\,\mathrm{m}^{-3}$. The upper bound of 40% for $\hat{n}_e$ may be too high. If it is assumed to correspond to 10% for example, the power reaching the inner 1/2 of the plasma remains as high as about 60%, even at the highest density.

G. Conclusions

The kinetic equation describing IBW scattering from turbulence has been solved using a Monte Carlo direct sampling simulation. The radial power deposition profile has been calculated as a function of edge density fluctuation amplitude and it is found that this power deposition profile is dependent on the normalized fluctuation amplitude $\hat{n}_e$. When there are no fluctuations present, the power is mainly deposited in the central plasma region where $\rho/a \leq 0.5$. A value of $\hat{n}_e \simeq 0.3$ is sufficient to broaden the power deposition profile and significantly reduce the IBW power reaching the central plasma. An upper bound on the measured value of $\hat{n}_e = 0.4$ at $\bar{n}_e = 3 \times 10^{20}\,\mathrm{m}^{-3}$ gives a decrease of about a factor of four in the

wave power which reaches the inner half of the plasma ($\rho/a \leq 0.5$) as the density increases from $\bar{n}_e = 1 \times 10^{20}\,\mathrm{m}^{-3}$ to $\bar{n}_e = 3 \times 10^{20}\,\mathrm{m}^{-3}$. A lower peak value of $\hat{n}_e$ at $\bar{n}_e = 3 \times 10^{20}\,\mathrm{m}^{-3}$ would produce less broadening of the power deposition profile. Although broadening of the power deposition profile in itself can only account for a fraction ($\sim$ 20–30%) of the ion heating rate decrease, the scattering results provide a method for determining the expected rf power deposition profile as a function of plasma density. This profile can now be used to describe the rf ion power source in a particle and energy transport model. This is carried out in the following section.

IV. Plasma Power Balance Analysis

A. Introduction

It has been shown previously that at high densities, the global energy confinement time in Ohmically heated plasmas on Alcator departs from the lower density neo–Alcator scaling $\tau_E \propto \bar{n}_e R^{2.04} a^{1.04}$ and becomes saturated [6, 22,23] . An anomaly in the ion thermal diffusivity, χ_i of three to five times greater than the Chang–Hinton neoclassical prediction is sufficient to account for the observed confinement behavior in these high density plasmas. To understand the effect of plasma energy confinement on the rf heating rate it is important to analyze the power balance in the rf heated discharges. This section describes the model used to analyze the plasma power balance and presents the results and interpretation of this analysis when applied to a set of IBW heated discharges. Only data at the 7.6 T and 9.3 T magnetic field regimes is analyzed; the changes in plasma parameters during rf injection at the 5.1 T regime are within experimental error and therefore no conclusions can be drawn from this data.

This section begins by describing the model used for the time dependent transport analyses. The model is then used to analyze the Ohmic portion of a set of discharges in both the 7.6 T and 9.3 T field regimes. The goal of the analyses is to understand the ion behavior. The electron behavior is only monitored due to its

necessity in calculating the electron–ion collisional power flow. The analyses show that in both magnetic field regimes, anomalous ion thermal conduction, relative to the neoclassical value, is required to explain the observed Ohmic ion temperature behavior and this anomaly increases with plasma density. The discharges are then analyzed during rf power injection. The fraction of rf power assumed to be deposited in the plasma is estimated from measured ion temperature profiles to be between 30% and 60% of the total rf power entering the antenna system. The rf power deposition profile is obtained from the scattering results given in section III. The results of the transport analyses indicate that the ion temperature behavior during rf power injection at 9.3 T can be explained by assuming that the ion thermal conductivity remains nearly equal to the value in the Ohmic portion of the discharge. The ion temperature behavior at 7.6 T during rf power injection can be explained by assuming that the ion thermal conductivity remains nearly Ohmic–like but increases slightly at low densities and may decrease some at high densities. These results suggest that at 7.6 T, the ion losses are typically enhanced at low densities at the onset of rf power injection; at high densities, the ion losses may be reduced. At the 9.3 T field regime, ion losses are typically maintained at the onset of rf power injection except at the highest densities. This contrasting behavior between the two field regimes may be caused by the differing power deposition profile in both field regimes and by the characteristics of the ion temperature gradient driven instability.

B. Analysis Technique

Energy and particle transport analysis of the data is carried out using a modified version of the ONETWO [6] transport code. Inputs for this code are the parameterized electron and ion temperature profiles, electron density profile, plasma current, Z_{eff}, and the resistive loop voltage, which are supplied at usually 9 and up to 19 instants of time before and during the time of rf power injection. The ion thermal conductivity is assumed to have the neoclassical form [24] and the code

determines an anomalous conduction factor which reproduces the measured central ion temperature.

Since an accurate measurement of the electron density profile was not available for the IBW experimental data, the profile was approximated as a parabola to the power α_n where α_n is adjusted to give the measured ratio of central to line–averaged density. Thus, α_n is given by

$$\frac{\bar{n}_e}{n_{e0}} = \frac{\sqrt{\pi}}{2} \frac{\Gamma(\alpha_n + 1)}{\Gamma(\alpha_n + \frac{3}{2})} \tag{9}$$

where $\Gamma(x)$ is the standard Gamma function. In most of the density interferometer data, only three of the interferometer chords which passed through the small size plasma recorded a signal above the noise level. Abel inverting these chord measurements to obtain a profile provided no better accuracy than the parabolic approximation.

The electron temperature profile was also approximated due to the lack of profile measurements. The T_e profile was assumed to be a parabola to the power α_T. An estimate of the value of α_T can be obtained in terms of the plasma central and edge safety factor $q = \rho B_0/(R_0 B_p)$ as

$$\alpha_T = \frac{2}{3}\left[\frac{q(a)}{q(0)} - 1\right]. \tag{10}$$

Equation (10) is obtained assuming that the Ohmic heating electric field E_0 and the value of Z_{eff} are uniform across the plasma.

The physical processes included in the power balance analysis are ion and electron heat transport, particle transport, magnetic diffusion, neutral transport, and radiation. The analysis is carried out in 1–D geometry (all quantities are functions only of time and the space coordinate ρ) assuming concentric flux surfaces. The diffusion equations considered in the transport model are

$$\frac{\partial n_e}{\partial t} + \frac{1}{\rho}\frac{\partial}{\partial \rho}\rho\Gamma_e = S_e \tag{11}$$

$$\frac{3}{2}\frac{\partial}{\partial t}n_e T_e = \frac{1}{\rho}\frac{\partial}{\partial \rho}\rho\left[n_e\chi_e\frac{\partial T_e}{\partial \rho} - \frac{5}{2}T_e\Gamma_e\right] + P_{\rm Oh} - P_{ei} - P_{\rm rad} + \frac{\Gamma_e}{n_e}\frac{\partial}{\partial \rho}\sum_{j=\rm ion} n_j T_i \tag{12}$$

$$\frac{3}{2}\frac{\partial}{\partial t}\sum_{j=\rm ion} n_j T_i = \frac{1}{\rho}\frac{\partial}{\partial \rho}\rho\left[\sum_{j=\rm ion} n_j\chi_i\frac{\partial T_i}{\partial \rho} - \frac{5}{2}T_i\sum_{j=\rm ion}\Gamma_j\right] + P_{ei} - P_{\rm cx} + P_{\rm rf} - \frac{\Gamma_e}{n_e}\frac{\partial}{\partial \rho}\sum_{j=\rm ion} n_j T_i \tag{13}$$

$$\frac{1}{c}\frac{\partial B_\theta}{\partial t} = \frac{\partial E}{\partial \rho}. \tag{14}$$

Here, $\Gamma_{e,i}$ is the electron or ion radial particle flux; S_e is the electron source rate (from all processes); $\chi_{e,i}$ is the electron or ion thermal diffusivity (the thermal conductivity is $\kappa_j = n_j\chi_j$); $P_{\rm Oh}$ is the Ohmic heating power density. The collisional power exchange between the electron and ions, P_{ei}, is given by

$$P_{ei} = \frac{3}{2}n_e\sum_{j=\rm ion}\nu_{ej}^{E}(T_e - T_j) \tag{15}$$

where

$$\nu_{e,j}^{E} = \frac{2m_e}{m_j}\frac{4}{3}\sqrt{\pi}\frac{n_j Z_j^2 e^4 \ln\Lambda}{\sqrt{m_e}T_e^{3/2}}; \tag{16}$$

$P_{\rm rad}$ is the local radiated power density, and $P_{\rm cx}$ is the charge exchange loss. The last term on the right side of Eqs. (12) and (13) represents an additional power exchange between the ions and the electrons [25] and is typically small compared to the other terms.

Boundary conditions for the electron and ion temperature and density are taken from plasma edge and scrape–off measurements. The total plasma current is used as the boundary condition for the magnetic diffusion equation.

A single impurity species is assumed to be present, either oxygen or molybdenum. The electron and ion fluxes are assumed ambipolar and are related as

$$\Gamma_e = \sum_{j=\text{ion}} Z_j \Gamma_j. \tag{17}$$

The impurity temperature is set equal to the main ion species temperature. The total source rate S_e, in Eq. (11), is determined with the help of a neutral transport package. An input value for the global particle confinement time τ_p^{in} provides the necessary boundary condition for the source calculation. Radiated power is calculated for bremsstrahlung and line radiation due to the assumed impurity species.

The magnetic diffusion equation is solved assuming classical resistivity and using the total plasma current input $I_p(t)$ as the boundary condition. The value of Z_{eff} is adjusted to match the experimental loop voltage. The resulting value can then be compared with the measured value for consistency. The measured inputs are averaged over any sawtooth effects, thus the calculated values of the transport coefficients include the time averaged effects of sawteeth. For the majority of discharges analyzed, the $q = 1$ surface is approximately at the magnetic axis of the plasma $[q(\rho = 0) \simeq 1]$.

The ion heat transport equation is solved assuming an ion thermal diffusivity of the form

$$\chi_i(\rho, t) = W(t)\chi_i^{\text{neo}}(\rho, t) + D_b f(q) \tag{18}$$

where $\chi_i^{\text{neo}}(\rho, t)$ is the Chang–Hinton neoclassical diffusivity, $D_b = ckT_i/16eB$ is the Bohm diffusivity, and

$$f(q) = \begin{cases} 1 - \frac{1}{1+(\frac{1}{q}-1)^2} & q \leq 1 \\ 0 & q > 1 \end{cases} \tag{19}$$

is used to model the time–averaged effect of sawtooth activity. The time dependent anomaly factor $W(t)$ is dynamically adjusted to reproduce the measured central ion temperature and the ion temperature profile is determined by the transport equations.

C. Anomalous Ion Thermal Conduction

The ion thermal conduction anomaly is essentially an indication of how different the measured ion temperature is from the expected value based on neoclassical theory. Typically, ion power losses are anomalously high causing the measured ion temperature to be lower than expected and to depart from the expected profile shape. To analytically investigate the effect of anomalously low ion temperature on the the neoclassical multiplier W, it is useful to construct an approximate analytic expression for W. This can be obtained by considering the power balance near the magnetic axis. Since the form of the ion thermal conductivity is assumed to be neoclassical and W is adjusted so as to give the central ion temperature, it is the characteristics of the transport near the plasma center which should be considered in determining the value of W. The value of $q(0)$ is assumed to be greater than or equal to unity in this analysis (*i.e.* there are no sawteeth present in the discharge).

Near the magnetic axis, especially at $\rho = 0$, the limiting value of the Chang–Hinton neoclassical ion thermal conductivity $\chi_i^{\rm neo}$ is written as

$$\chi_i^{\rm neo}(0) = q\frac{K_2^{(0)}}{b_2}\frac{1}{\sqrt{2}R_0}\frac{v_{ti}^3(0)}{\Omega_{i0}^2} \tag{20}$$

where Ω_{i0} is the gyrofrequency evaluated using the toroidal field on axis and $K_2^{(0)}$ and b_2 are numerical constants. This region near the magnetic axis is not pathological since its size is much larger than an ion cyclotron radius at a toroidal magnetic field of 7.6 T ($\rho_{\rm H} \simeq 0.06\,{\rm cm}$). Since the ion thermal diffusivity is explicitly independent of the collision frequency in this regime, it has no explicit $Z_{\rm eff}$ dependence [26] . Its main dependence is given by $T_j(0)^{3/2}/(Z_j B_0)^2$.

An approximate expression for W can be obtained by writing out the ion power balance at $\rho = 0$ as

$$W \simeq -P_{ei}|_{\rho=0} \Big/ \frac{1}{\rho}\frac{\partial}{\partial\rho}\rho\left[\sum_{j={\rm ion}} n_j \chi_i^{\rm neo}\frac{\partial T_i}{\partial\rho}\right]_{\rho=0} \tag{21}$$

where the charge exchange and convective power loss has been neglected [27] and i indicates the main ion species.

The expression for the electron–ion power flow is

$$P_{ei} \propto n_e(0) \sum_{j=\text{ion}} \left(\frac{Z_j}{\mu_j}\right) Z_j n_j(0) \ln \Lambda_{ej} \frac{T_e - T_j}{T_e^{3/2}} \tag{22}$$

where μ_j is the atomic mass number of the j ion species. The ratio Z_j/μ_j is unity for hydrogen and about $1/2$ for an impurity ion. A Z_{eff} different than unity has a minor effect on the behavior of P_{ei}, mainly by adjusting the ion species densities.

An estimate of $\partial^2 T_i(0)/\partial\rho^2$ is $T_i(0)/a_s^2$ where a_s is the ion temperature profile scale length. This gives an overall estimate for W of

$$W \propto \left(\frac{T_i^{\text{neo}}}{T_i}\right)^{5/2} \left(\frac{a_s}{a_s^{\text{neo}}}\right)^2 \frac{T_e - T_i}{(T_e - T_i)^{\text{neo}}}. \tag{23}$$

Equation (23) shows that within the previous approximations, anomalous plasma transport, which is indicated by a value of $W > 1$, will cause the plasma characteristics to depart from the expected neoclassical behavior in three ways. First, the central ion temperature may decrease. Second, the ion temperature profile may broaden. Third, the collisional power flow into the ions may change depending on how the electron temperature responds to the anomalous transport. If the ion temperature profile and the collisional power flow into the ions is only weakly affected by the anomalous transport processes, the value of W is then essentially an indication of how different the measured central ion temperature is from the expected neoclassical value.

D. Ohmic Discharges at 7.6 Tesla

Analysis at the 7.6 T regime was done for 14 discharges which spanned a density range of $0.75\times10^{20}\,\text{m}^{-3} \leq \bar{n}_e \leq 2.8\times10^{20}\,\text{m}^{-3}$. Figure 7 (a) shows the inferred value of the ion thermal conduction anomaly in the Ohmically heated portion of these discharges as a function of the line–averaged density. The total plasma current

ranges between 230 kA and 290 kA with an Ohmic input power $P_{Oh} = 550 \pm 100$ kW. The value of Z_{eff} is shown in Fig. 7 (b) and exhibits the behavior of a decreasing value with increasing density. The ratio of central to line–averaged density is typically about 1.2–1.4 (corresponding to $\alpha_n \simeq 0.6$) indicating a broad density profile. The ion conduction anomaly is nearly constant at a value close to unity (within the error) for low density discharges but then begins to increase with density. The absolute magnitude of the neoclassical ion thermal diffusivity [calculated from the measured values of $n_j(0)$ and $T_j(0)$] on the magnetic axis is typically about 3000 cm^2/s and ranges from 2600 cm^2/s to 5000 cm^2/s.

Figure 8 shows the individual components of the integrated ion power flow at $\rho/a = 0.75$. Each power shown is normalized to the total integrated Ohmic input power at $\rho/a = 0.75$. Most of the power flow important to the description of these discharges appears to take place within $\rho/a = 0.75$. Limiting the analysis to within this region excludes the power flow in the edge region which can be dominated by errors resulting from uncertainties in the boundary values. The power loss through convection is typically about $0.1\,P_{Oh}$ and remains relatively independent of density. The power loss through charge exchange plus ionization is less than $0.05\,P_{Oh}$ and decreases from a positive value to a negative value with density. The power loss through conduction increases nearly linearly with density and follows the electron–ion power source which also increases with density. The conduction and convection power losses are comparable for $\bar{n}_e \leq 1.5 \times 10^{20}$ m^{-3}. In this region, improvements in the particle confinement time can have a significant effect on the overall ion power balance. At higher densities, the particle confinement time is not as important.

E. Rf Heated Discharges at 7.6 Tesla

The rf power source is modeled in the shape of an annulus with power distributed across the annulus area according to the power deposition profile estimated from the scattering results (see Figs. 4 and 5). The fluctuation amplitude is assumed to be within the range 0–40% at $\bar{n}_e = 3 \times 10^{20}$ m^{-3}. The total rf power

which actually flows into the hydrogen comes from both collisional power exchange from the heated deuterium and possibly from direct rf power absorption on the hydrogen. The power flow from the heated deuterium to the hydrogen has been estimated from measured profiles of the hydrogen and deuterium temperatures to be $\sim 0.3\,P_{rf}$. The maximum power available for heating the plasma is $0.65 - 0.75\,P_{rf}$. This power fraction is obtained by comparing the vacuum loading resistance with the plasma loading resistance. The power deposited directly into the hydrogen cannot be obtained from the data; however, an upper and lower limit to this value can be estimated from the characteristics of the absorption mechanism. On one hand, if rf power absorption occurs primarily via IBW parametric decay, the maximum power flow into the hydrogen can be the maximum available power $(0.65 - 0.75\,P_{rf})$. The details of this power flow may be as follows. The quasimode at $\omega = 0.5\Omega_H$, which is absorbed by the deuterium, contains $\sim 0.2\,P_{rf}$. The lower frequency IBW at $\omega = (1+x)\Omega_H$ $(x << 1)$, which contains $\sim 0.4\,P_{rf}$ (this fraction is estimated from the Manley–Rowe nonlinear energy relations [28]), is absorbed directly by the hydrogen. The total power flow from the deuterium to the hydrogen is $0.3\,P_{rf}$, therefore an additional linear power absorption of $0.1\,P_{rf}$ by the deuterium is required. This places an upper bound on the total power which flows into the hydrogen at $\lesssim 0.75\,P_{rf}$. On the other hand, if rf power absorption on the deuterium occurs only via linear damping at the $\omega = 3\Omega_D$ layer, it is possible that no power is absorbed directly by the hydrogen via self–interaction near $\omega = 1.5\Omega_H$. In this case, the total power which flows into the hydrogen is $\sim 0.3\,P_{rf}$ and comes only from the heated deuterium. The total power flow into the hydrogen at 7.6 T lies within the range $0.3 - 0.75\,P_{rf}$. In order to make the comparison with the results at 9.3 T straightforward, a power flow within the range $0.3 - 0.6\,P_{rf}$ was used to model the rf portion of the discharges at this field regime. Increasing the upper bound to $0.75\,P_{rf}$ does not produce significant changes in the results obtained for $0.6\,P_{rf}$.

Figure 9 (a) shows a comparison of the inferred value of the ion thermal conduction anomaly during the Ohmic heated portion of the discharge with the anomaly

during the Ohmic and IBW heated portion. The letters label points corresponding to the same discharge. Notice that at low densities, the density during rf power injection is somewhat higher than during the Ohmic heating phase. Assuming that $0.3 - 0.6\,P_{rf}$ flows into the hydrogen, the ion thermal conduction anomaly can remain nearly Ohmic–like to explain the observed ion temperature behavior. There is a small increase in the ion thermal conduction at low densities (by a factor of $\lesssim 2$) which is nearly outside of the error bars. This may indicate that χ_i degrades at the onset of rf power injection at low densities. At higher densities, χ_i appears to improve although the improvement is within the error bars. The error bars in this case include both uncertainties in the plasma parameters and uncertainty in the power flow to the hydrogen.

Several cases were studied which attempt to isolate the effects of uncertainty in both the amplitude of the total power which flows into the hydrogen and in the edge density fluctuation amplitude. Each case studied is constructed assuming that the rf power and the fluctuation amplitude is a known quantity so that only uncertainties in the plasma parameters are represented by the error bars. Comparisons among the different cases indicate the separate effects of the uncertainties in power flow and fluctuation amplitude. Figure 9 (b) shows the result of assuming that $0.6\,P_{rf}$ flows into the hydrogen and the fluctuation amplitude is 40% at $\bar{n}_e = 3 \times 10^{20}\,\mathrm{m}^{-3}$. The effect of reducing the total power to $0.3\,P_{rf}$, while keeping the fluctuations the same, is shown in Fig. 10 (a). The figure shows that the ion thermal conductivity can still remain nearly Ohmic–like to explain the ion temperature increase. The slight increase in the ion thermal conductivity at low densities is $\lesssim 1.5$ times and the decrease at high densities is more significant. This result still suggests that the ion thermal conduction may increase slightly at low densities and decrease at high densities. The effect of reducing the fluctuation amplitude to 0% while keeping the power flowing into the hydrogen at $0.6\,P_{rf}$ is shown in Fig. 10 (b). The rf power is mainly deposited between $1\,\mathrm{cm} \leq \rho \leq 4\,\mathrm{cm}$ without edge fluctuations. The ion thermal conductivity for this case shows a large increase (2–4 times the Ohmic

value) at low densities and is relatively unchanged at high densities. If this power deposition model is correct, then the ion losses are strongly enhanced at the onset of rf power injection at low densities but are not changed from an already large value at high densities.

Several types of ion temperature simulations were made with the data at $B_0 = 7.6\,\mathrm{T}$. The main purpose of these simulations is to see if the ion temperature behavior can be explained by changes in the confinement time alone, with no rf power flow to the ions. A simulation is carried out by assuming a constant value for the ion thermal conduction anomaly W_{sim} and simulating the central ion temperature behavior. The anomaly used to simulate the rf portion of the discharges is assumed to be Ohmic–like [see Fig. 7 (a)]. In most of the 7.6 T cases the density increase at the onset of rf power injection was small ($\lesssim 20\%$) and W_{sim} was set to be nearly equal to the initial Ohmic value. The cases with $W_{\mathrm{Oh}} \lesssim 1$ had the largest density increases and showed a large increase in the value of W. These cases were simulated with $W_{\mathrm{sim}} = 1.5$. Figure 11 shows the results of two simulations of $\Delta T_i/P_{\mathrm{rf}}$ compared with the experimentally measured value. The first simulation is made by assuming that no rf power flows into the ions but that the ion temperature increase results only from an improvement in the global particle confinement time so that $\tau_p(\mathrm{rf}) = 1.5\tau_P(\mathrm{Oh})$ (independent of density). The measured behavior of $\tau_p(\mathrm{rf})/\tau_p(\mathrm{Oh})$ decreases with density, therefore this simulation represents an approximate upper bound to the ion heating rate resulting only from a τ_p improvement. Another simulation, not shown in Fig. 11 , was done assuming that $\tau_p(\mathrm{rf}) = 2\tau_p(\mathrm{Oh})$; in these cases, the simulated value of $\Delta T_i/P_{\mathrm{rf}}$ was approximately twice that for $\tau_p(\mathrm{rf}) = 1.5\tau_p(\mathrm{Oh})$. The second simulation shown in Fig. 11 is made by assuming that both the global particle confinement time improves as in the first simulation and that $0.6\,P_{\mathrm{rf}}$ is deposited into the main ions in a radial profile given by the scattering results (assuming that $\hat{n}_e = 0.4$ at $\bar{n}_e = 3 \times 10^{20}\,\mathrm{m}^{-3}$). In both simulations, the value of P_{rf} used to calculate the quantity $\Delta T_i/P_{\mathrm{rf}}$ is the total measured rf power entering the antenna system under matched conditions and ΔT_i is

the difference in ion temperature between the already described simulation and a *baseline* simulation where $P_{rf} = 0$, $\tau_p(\mathrm{rf}) = \tau_p(\mathrm{Oh})$, and $W = W_{sim}$. The simulations confirm that a nonzero source of rf power is required to explain the measured ion temperature behavior provided that the ion thermal conduction doesn't decrease relative to the Ohmic value at the onset of rf power injection.

Ion heating rate simulations of the data at $B_0 = 7.6\,\mathrm{T}$ exhibit two important characteristics. First, both simulations show a strong decrease in the ion heating rate as a function of density. This results almost entirely from the increasing ion thermal conduction anomaly. In the first simulation where $P_{rf} = 0$, the power loss due to ion conduction quickly becomes the dominant ion loss mechanism as the density increases. As a result, decreasing the convection loss by improving τ_p produces an increasingly smaller effect on the ion power balance. In the second simulation where $0.6\,P_{rf}$ flows into the hydrogen, the increasing anomalous ion conduction loss reduces the ion energy confinement resulting in less of an ion temperature increase for a given rf input power.

The second characteristic is that the simulated heating rate at low densities (assuming an Ohmic–like ion thermal conduction) is somewhat greater than the measured rate at low densities. However, at higher densities, the simulated heating rate is slightly less than the measured heating rate. A similar result occurs if a lower power flow into the hydrogen of $0.3\,P_{rf}$ is assumed. A lower power flow of $0.3\,P_{rf}$ will reduce the simulated heating rate at all densities but not enough to match the data at the lowest densities ($\Delta T_H/P_{rf} \sim 2.5 - 3\,\mathrm{eV/kW}$ at the lowest densities). The interpretation of this result is that at low densities, rf power injection enhances the ion losses so as to degrade the ion thermal conduction from its Ohmic–like value to a value which is 2–3 times the neoclassical value. The ion thermal conduction at high densities is slightly reduced from its Ohmic–like value at the onset of rf power injection. This interpretation is consistent with the results shown in Fig. 9 (a). Assuming that either the fluctuation amplitude or the total power which flows into the hydrogen is overestimated does not qualitatively change this interpretation. At

the onset of rf power injection, the low density discharges still show an increase in the Ohmic–like ion thermal conduction and the high density discharges still show either a slight decrease or no change from the Ohmic–like value.

Summarizing the results at 7.6 T, it is shown that within experimental uncertainty, the inherent ion energy confinement in these discharges can explain the ion temperature behavior. More specifically, assuming that $0.3 - 0.6\,P_{rf}$ flows into the hydrogen with a radial profile given by the scattering results, the ion thermal conductivity must increase by $\lesssim 1.5$ times the Ohmic value (to 2–3 times the Chang–Hinton neoclassical prediction) at the onset of rf power injection to explain the ion temperature behavior in the low density discharges. At high densities, the Ohmic ion thermal conductivity is already 4–7 times the Chang–Hinton neoclassical value and may decrease slightly at the onset of rf power injection.

F. Ohmic Discharges at 9.3 Tesla

Analysis at the 9.3 T regime was done for 8 discharges which spanned a density range of $0.8 \times 10^{20}\,\mathrm{m}^{-3} \leq \bar{n}_e \leq 2 \times 10^{20}\,\mathrm{m}^{-3}$. These discharges showed qualitatively similar behavior as the 7.6 T data; however, there were some marked differences. Figure 12 (a) shows the inferred value of the ion thermal conduction anomaly of the Ohmic portion of the discharges as a function of line–averaged density. The Ohmic power is 450 ± 60 kW. This is slightly lower than the 7.6 T data due to a lower plasma current (~ 180 kA) and a slightly lower resistive loop voltage. The density dependence of Z_{eff} is shown in Fig. 12 (b). The ratio of central to line–averaged density is 1.4–1.9 ($\alpha_n \sim 1.6$) indicating a somewhat more peaked density profile than in the 7.6 T discharges. The ion thermal conduction anomaly is small (1–2 times the Chang–Hinton neoclassical prediction) at low densities and shows an increase at higher densities. The absolute magnitude of the neoclassical ion thermal diffusivity on the magnetic axis in these discharges is somewhat smaller ($2300\,\mathrm{cm}^2/\mathrm{s}$) than in the 7.6 T cases.

The individual components of the ion power flow are shown in Fig 13 (a). The power is integrated out to $\rho/a = 0.5$ since most of the power flow in these discharges seems to occur within this region. This slightly smaller region, as compared to the 7.6 T regime, is probably a consequence of the more peaked profiles at higher q. The integrated power at $\rho/a = 0.75$ is shown in Fig. 13 (b) for comparison. Convective power loss is typically less than $0.1\,P_{\rm Oh}$. Power loss through charge exchange and ionization is less than $0.05\,P_{\rm Oh}$. The conductive power loss increases with density and follows the electron–ion power source. Within $\rho/a \leq 0.75$, the convective and conductive power losses are comparable indicating that particle confinement improvements can influence the ion power flow for nearly all of the cases considered.

G. Rf Heated Discharges at 9.3 Tesla

At this magnetic field, rf power absorption is expected to occur on deuterium and hydrogen at the $\omega = 3\Omega_{\rm D}$ layer located $\lesssim 2\,$cm in front of the antenna and on the deuterium at the $\omega = 2.5\,\Omega_{\rm D}$ layer located near the center of the plasma. Direct power absorption on the hydrogen in the plasma center is not expected. The central power flow into the deuterium has been estimated from the hydrogen and deuterium temperature profiles to be 20 kW–40 kW or $0.3 - 0.6\,P_{\rm rf}$ [29] ; the primary uncertainty in making this estimate lies in the value of the deuterium concentration. The fraction of power deposited near the plasma edge at the $\omega = 3\Omega_{\rm D}$ layer cannot be determined from the data but can be estimated from theoretical considerations. If rf power crosses the $\omega = 3\Omega_{\rm D}$ layer via parametric decay, the lower frequency IBW at $\omega \simeq 2.8\,\Omega_{\rm D}$, which is eventually absorbed by the deuterium in the plasma center, must contain (from profile data) $0.3 - 0.6\,P_{\rm rf}$. The quasimode at $\omega \simeq 0.2\,\Omega_{\rm D}$ contains $0.02 - 0.05\,P_{\rm rf}$ (estimated from the Manley–Rowe nonlinear energy relations [28]). The remaining power, $0.35 - 0.7\,P_{\rm rf}$, is possibly deposited near the plasma edge at the $\omega = 3\Omega_{\rm D}$ layer. If rf power crosses the $\omega = 3\Omega_{\rm D}$ layer due to the toroidal ripple effect on the resonance layer location [2] , the power flow into the deuterium must still be $0.3 - 0.6\,P_{\rm rf}$ and the power deposited at the plasma edge in this case may be 0.4 –

$0.7\,P_{rf}$. Power conducted out by the high energy deuterium component is estimated to be negligible due to the low deuterium density. In view of these considerations, a central power flow of $0.3 - 0.6\,P_{rf}$ into the hydrogen from the heated deuterium was assumed to model the rf portion of these discharges.

The rf power source for this regime is also modeled in the shape of an annulus with the power distributed according to the estimated power deposition profile. Once power crosses the $\omega = 3\Omega_D$ layer, ray tracing calculations at this field give a power deposition profile similar to the 7.6 T regime. Edge density fluctuations, measured for $\bar{n}_e > 1 \times 10^{20}\,m^{-3}$, are observed at 9.3 T; the measurements show a nearly identical behavior as is observed in the 7.6 T regime [see Fig. 3 (b)]. The fluctuation amplitude is assumed to be within the range 0–40% at $\bar{n}_e = 3 \times 10^{20}\,m^{-3}$. Figure 14 (a) shows a comparison of the inferred value of the ion thermal conduction anomaly during the Ohmic heated portion of the discharge with the anomaly during the Ohmic and IBW heated portion. The data points are plotted at the line–averaged density corresponding to either the Ohmic or the Ohmic and IBW heated portion of the discharge. Assuming that $0.3 - 0.6\,P_{rf}$ flows into the hydrogen, an ion thermal conduction anomaly during rf power injection which is approximately equal to the Ohmic value, is sufficient to explain the ion temperature behavior. This is in contrast to the 7.6 T data at low densities which showed that a small increase in the ion thermal conduction during rf power injection is necessary to account for the ion temperature behavior.

As in the 7.6 T regime, several cases were studied which attempt to isolate the effects of uncertainty in both the amplitude of the total power which flows into the hydrogen and in the edge density fluctuation amplitude. These cases were constructed by assuming that the power flow and fluctuation amplitude is a known value within the range of uncertainty, chosen to correspond to the cases studied at 7.6 T. Comparisons among these cases and those at 7.6 T show the separate effects of the uncertainties and indicate the differences between the two magnetic field regimes. Figure 14 (b) shows the result of assuming that $0.6\,P_{rf}$ flows into

the hydrogen and that the fluctuation amplitude is 40% at $\bar{n}_e = 3 \times 10^{20}\,\mathrm{m}^{-3}$. The effect of reducing the total power to $0.3\,P_{rf}$, while keeping the fluctuations the same, is shown in Fig. 15 (a). The figure shows that the ion thermal conductivity decreases slightly from the Ohmic value at the onset of rf power injection. This result suggests that the ion losses are reduced in comparison to the initial Ohmic losses at the onset of the rf power. The effect of reducing the fluctuation amplitude to 0% while keeping the power flowing into the hydrogen at $0.6\,P_{rf}$ is shown in Fig. 15 (b). In this case, the ion thermal conduction can remain nearly Ohmic–like to explain the ion temperature behavior. In each case, the results at the 9.3 T regime indicate that the ion losses are either reduced as compared with, or maintained at the Ohmic values at the onset of rf power injection.

Figure 16 shows the result of an ion temperature simulation where the particle confinement is assumed to improve in accord with the data [2] and $0.6\,P_{rf}$ is assumed to flow into the hydrogen with a profile approximated from the scattering results. The ion thermal conduction anomaly is assumed to be Ohmic–like. The particle confinement improvement can explain up to $\sim 50\%$ (at low densities) of the observed ion temperature behavior; however, a nonzero amount of rf power is required to account for the complete ion temperature behavior. A number of the low density discharges (one is included with the 8 cases analyzed here) with the highest ion heating rate showed a slight peaking of the density profile during rf power injection.

The measured ion heating rate for several of the high density ($\bar{n}_e \geq 2 \times 10^{20}\,\mathrm{m}^{-3}$) discharges was typically ≤ 0. This resulted because at the onset of rf power injection, the electron temperature decreased markedly. At high densities, since the electrons and ions are strongly coupled, the ion temperature fell below its Ohmic value in response to the electron temperature. The electron temperature behavior resulted from impurity generation, an increase in the ion thermal conduction, and a possible increase in the electron thermal conduction at the onset of rf power injection. Since T_e and T_i are measured, we can infer an increase in χ_i; however, since accurate impurity radiation measurements are unavailable, χ_e is not known.

The rf power is typically $P_{rf} \geq 110\,\mathrm{kW}$ for these discharges and impurity generation increases with rf power and plasma density.

The ion heating rate simulation at 9.3 T shows a strong decrease as a function of density and is similar in magnitude to the 7.6 T data indicating that the Ohmic ion heating rate of the two magnetic field regimes is nearly the same. The decrease in ion heating rate with density results once again from the increasing ion thermal conduction anomaly. The simulated ion heating rate is typically lower than the measured heating rate. The interpretation of this result is that Ohmic–like ion thermal conduction during rf power injection used in the simulation is too large. This is consistent with the results shown in Figs. 14 and 15 . The ion losses are either reduced relative to, or maintained at the Ohmic values at the onset of rf power injection.

Summarizing the results at 9.3 T, it is shown that the inherent Ohmic ion energy confinement which is characteristic of these discharges can account for the observed ion temperature behavior. In particular, assuming that $0.3 - 0.6\,P_{rf}$ flows into the hydrogen in a power deposition profile given by the scattering calculation, an ion thermal conduction similar to the Ohmic value is sufficient to explain the observed ion temperature behavior during rf power injection. Uncertainties in the edge density fluctuation amplitude and in the total power flowing into the hydrogen do not qualitatively alter this conclusion.

H. Sensitivity of Simulation Results

Uncertainties in the experimental parameters can alter the results of the power balance analyses. To determine the effects of the uncertainties, several test discharges were constructed by varying the measured quantities of actual discharges within the limits of experimental error. The primary sources of error are in the electron central temperature and profile, electron central density and profile, and the absolute value of the particle confinement time τ_p. The error in the central value

of T_e is estimated to be about 10% [6] . The error in central electron density measured from the Thompson scattering system is estimated to be about 15% and the error in the calculated density profile is taken to be 15%. The error in the absolute magnitude of τ_p is roughly estimated to be about 50%. The resulting variation in the inferred ion thermal conductivity and the simulated ion heating rate is shown by the error bars. The uncertainty in χ_i/χ_i^{neo} is small at low densities and large at high densities. At low densities, the electrons and ions are not well coupled since the difference in their temperatures is large. A 10%–15% change in the electron temperature and density does not produce a large effect on the ions. This situation changes at high densities where the electron and ion temperatures are much closer together and the value of P_{ei}, which mainly influences the value of W, is very sensitive to variations in T_e. Within the experimental error it can still be concluded that the ion thermal conduction anomaly in these discharges increases with density.

I. Discussion

Previous authors [6, 22, 30, 31] have indicated the presence of anomalous ion thermal conduction in the Alcator C tokamak and have shown that the anomaly increases with plasma current. In addition, experiments on other tokamaks suggest the existence of anomalously high ion losses and associate these losses with the density profile shape [32] . The results of the analyses of the IBW data on Alcator C show that the anomaly also increases with increasing plasma density.

It has been suggested that the cause of the anomalous ion thermal conduction may arise from ∇T_i–driven ion drift instabilities (*e.g.* the ion mixing mode or η_i mode). This instability has been discussed by a number of authors [4, 5, 33–36] and arises from ion drift modes which tend to mix hot and cold ion populations. The mode becomes unstable when η_i exceeds a critical value η_{crit} where

$$\eta_i \equiv \frac{d(\ln T_i)}{d(\ln n_i)}. \tag{24}$$

and $\eta_{crit} \sim 1.5$. The mode tends to be excited by a combination of a broad ion density profile and a narrow ion temperature profile.

The measured ion temperature and density profiles contain significant errors and unfortunately cannot be used to estimate a meaningful value of η_i. Nevertheless, previous estimates on Alcator C [6] indicate that $0.8 \leq \eta_i(a/2) \leq 1.7$ for gas fueled discharges. It is interesting to estimate an upper bound for χ_i due to the enhanced transport from ion temperature gradient driven modes. One estimate for the ion thermal diffusivity has been given in Ref. 31 as

$$\chi_i \approx T^2 \left(\frac{\rho_i}{r_T}\right)\left(\frac{qR}{r_T}\right)\left(\frac{cT_i}{eB}\right)F(r) \tag{25}$$

where $r_T^{-1} = d(\ln T_i)/d\rho$, ρ_i is the ion gyro–radius, $2\pi Rq$ is the relevant connection length, T is of order unity, and $F(r)$ is a function which represents the spatial dependence of the amplitude. Estimating this near $\rho/a \sim 0.5$ for either magnetic field regime for $F \sim 1$ gives a value for χ_i which is 20–100 times larger than the neoclassical value. This result additionally confirms the possibility of enhanced transport due to ion temperature gradient driven modes.

The behavior of the rf heated discharges at 7.6 T and 9.3 T may be understood in terms of the rf power deposition profile and the characteristics of the ion temperature gradient driven instability. For example, at low densities in the 7.6 T regime, rf power deposition is peaked near the plasma center ($1\,\text{cm} \leq \rho \leq 4\,\text{cm}$) since scattering effects are not significant. This may cause the ion temperature profile to peak in the center, increasing the value of η_i, and leading to an enhancement of the ion losses. At higher density, scattering effects cause the power deposition profile to become spread over the plasma cross–section. This may cause the ion temperature profile to increase in a more uniform way causing the value of η_i to remain nearly constant or possibly decrease. The ion thermal conduction then remains nearly constant or decreases in response. At the 9.3 T regime, rf power deposition may occur both at the plasma edge (at the $\omega = 3\Omega_D$ layer) and near the center of the plasma.

Power deposited at the plasma edge may broaden the ion temperature profile causing the value of η_i to decrease independently of the central power deposition profile. The ion thermal conduction then decreases or maintains an Ohmic–like value at the onset of rf power injection.

The different behavior of the rf heated discharges at 7.6 T and 9.3 T may indicate the importance of favorably modifying the ion temperature profile with rf power in order to improve energy confinement. The 9.3 T regime provides a natural way of doing this with the $\omega = 3\Omega_D$ layer located just in front of the antenna.

J. Global Energy Confinement

Figure 17 shows the global energy confinement time during the Ohmic heating phase and the Ohmic plus IBW heating phase for both field regimes. Although numerous discharges showed a global energy confinement time during rf power injection which was greater than the initial Ohmic value, the global energy confinement time during rf power injection was always less than the confinement time of an equivalent Ohmic discharge (at the same density) for both field regimes. The cause of this is partially due to increased radiation loss from impurities and partially due to degraded confinement. This is especially apparent in the 9.3 T data which shows large electron temperature decreases (particularly at higher densities) at the onset of rf power injection. The electron temperature also decreases in the 7.6 T data; however, the decrease is not as significant as in the 9.3 T data. As a result, the global energy confinement time during rf power injection is somewhat lower ($\tau_E \sim$ 8–10 ms) at 9.3 T than at 7.6 T ($\tau_E \leq 15$ ms).

K. Summary and Conclusions

Analyses of Ohmic discharges at 7.6 T and 9.3 T have indicated the presence of anomalous ion thermal conduction which increases with plasma density. This anomalous ion thermal conduction may be due to increased transport arising from η_i modes. The ion temperature behavior at 7.6 T can be explained by assuming that

$0.3 - 0.6\,P_{rf}$ is deposited into the hydrogen in a profile given by the scattering results. At low densities, the rf power deposition profile, which is peaked near the plasma center, may cause the ion temperature profile to peak. This may increase the value of η_i causing the ion thermal conductivity to increase above the Ohmic–like value. At higher densities, the power deposition profile is broadened as a result of the edge fluctuations causing the value of η_i to remain equal to the Ohmic value or possibly decrease. The result is that the ion thermal conduction remains nearly the same as the Ohmic value or decreases slightly. The ion temperature behavior at 9.3 T can be accounted for by assuming that $0.3 - 0.6\,P_{rf}$ is absorbed by the hydrogen in a profile given by the scattering results, and that the ion thermal conductivity remains nearly equal to the Ohmic value. Power deposition near the plasma edge at the $\omega = 3\Omega_D$ layer may broaden the ion temperature profile causing the value of η_i to decrease or remain constant. The ion thermal conduction then remains constant or decreases in response. The decrease in the ion heating rate with increasing density in both magnetic field regimes is essentially accounted for by the increasing anomaly in the ion thermal conductivity as a function of plasma density. Uncertainties in the total power flow into the hydrogen and in the fluctuation amplitude do not qualitatively alter these conclusions. Unfortunately, due to a lack of accurate ion density and temperature profile measurements, more definitive statements regarding η_i modes cannot be made.

Acknowledgements

One of the authors (J. D. M.) would like to thank Dr. P. T. Bonoli for many useful discussions concerning both the modeling of IBW scattering from density fluctuations and interpreting results of the transport studies. He would also like to thank Dr. Y. Takase for many helpful discussions regarding eta–i modes and these transport studies. Dr. S. Wolfe has helped with understanding the ONETWO transport code, and with discussions regarding particle transport. Dr. C. Fiore provided the ion temperature measurement in Fig. 2, and the data in Fig. 3 was

obtained by Dr. Y. Takase. Special thanks are due to Dr. B. Coppi and Dr. R. R. Parker for reading the thesis on which this present manuscript is based and for offering helpful comments and suggestions. This work was supported by the U. S. Department of Energy under Contract No. DE–AC02–78ET51013.

REFERENCES

1. M. ONO, in *Applications of Radio–Frequency Power to Plasmas–1987*, edited by S. Bernabei and R. W. Motley, AIP Conference Proceedings No. 159 (American Institute of Physics, New York, 1987), p. 230.
2. J. D. MOODY, M. PORKOLAB, C. L. FIORE, F. S. MCDERMOTT, Y. TAKASE, J. TERRY, AND S. M. WOLFE, *Phys. Rev. Lett.*, **60**, 298, (1988).
3. Y. TAKASE, J. D. MOODY, C. L. FIORE, F. S. MCDERMOTT, M. PORKOLAB, AND J. SQUIRE, *Phys. Rev. Lett.*, **59**, 1201, (1987).
4. M. PORKOLAB, *Physics Letters*, **22**, 427, (1966); also *Nucl. Fusion*, **8**, 29, (1968).
5. B. COPPI, M. N. ROSENBLUTH, AND R. Z. SAGDEEV, *Phys. Fluids*, **10**, 582, (1967).
6. S. M. WOLFE, M. GREENWALD, R. GANDY, R. GRANETZ, C. GOMEZ, D. GWINN, B. LIPSCHULTZ, S. MCCOOL, E. MARMAR, J. PARKER, R. R. PARKER, J. RICE, *Nucl. Fusion*, **26**, 329, (1986); W. W. PFEIFFER, R. H. DAVIDSON, R. L. MILLER: Private communication.
7. M. PORKOLAB AND J. D. MOODY, *Bull. Am. Phys. Soc.*, **32**, 1939, (1987).
8. M. PORKOLAB, *Phys. Rev. Lett.*, **54**, 434, (1985).
9. M. PORKOLAB, P. BONOLI, K-I. CHEN, C. FIORE, R. GRANETZ, D. GRIFFIN, D. GWINN, S. KNOWLTON, B. LIPSCHULTZ, S. C. LUCKHARDT, E. MARMAR, M. MAYBERRY, F. S. MCDERMOTT, J. D. MOODY, R. PARKER, J. RICE, Y. TAKASE, J. TERRY, S. TEXTER, S. WOLFE, in Plasma Physics and Controlled Nuclear Fusion Research 1986, Proceedings of the 11th International Conference, Kyoto (IAEA, Vienna, 1987), Vol. 1, p. 509.
10. M. BRAMBILLA, in *Application of Radio–Frequency Power to Plasmas–1987*, edited by S. Bernabei and R. W. Motley, AIP Conference Proceedings No. 159 (American Institute of Physics, New York, 1987), p. 406.
11. D. D. HARMS, *Nucl. Fusion*, **16**, 753, (1976).
12. R. L. WATTERSON, R. E. SLUSHER, AND C. M. SURKO, *Phys. Fluids*, **28**, 2857, (1985).
13. J. D. MOODY, Ph. D. Thesis, Massachusetts Institute of Technology, (1988).
14. JEROME SPANIER AND ELY M. GELBARD, *Monte Carlo Principles and Neutron Transport Problems*, (Addison–Wesley Publishing Company, Reading, Massachusetts, 1969).
15. P. T. BONOLI AND E. OTT, *Phys. Fluids*, **25**, 359, (1982).
16. M. ONO, *Phys. Fluids*, **25**, 990, (1982).
17. E. OTT, *Phys. Fluids*, **22**, 1732, (1979).

18. R. E. SLUSHER AND C. M. SURKO, *Phys. Rev. Lett.*, **37**, 1747, (1976).
19. M. BRAMBILLA AND A. CARDINALI, *Plasma Physics*, **24**, 1187, (1982).
20. The power *density* normalized to unity is given by the total power deposited in a bin P_j divided by $\rho_j S$ where ρ_j is the radial location of the bin and $S = \sum_j P_j/\rho_j$.
21. M. BRAMBILLA, Private communication, (1987).
22. R. R. PARKER, M. GREENWALD, S. C. LUCKHARDT, E. S. MARMAR, M. PORKOLAB, S. M. WOLFE, *Nucl. Fusion*, **25**, 1127, (1985).
23. B. D. BLACKWELL, C. L. FIORE, R. GANDY, A. GONDHALEKAR, R. S. GRANETZ, in Plasma Physics and Controlled Nuclear Fusion Research 1982, Proceedings of the 9th International Conference Baltimore, (IAEA, Vienna, 1983), Vol. 2, p. 27.
24. C. S. CHANG AND F. L. HINTON, *Phys. Fluids*, **29**, 3314, (1986).
25. F. L. HINTON AND R. D. HAZELTINE, *Rev. Mod. Phys.*, **48**, 239, (1976).
26. This is the case where particles which dominate the diffusion have a collision time which is on the order of the time it takes a circulating ion to complete one poloidal orbit. Thus, the collision frequency ν_{ei} can be approximately replaced with $1/\tau_c$ where τ_c is the period for one complete poloidal orbit. This time is only dependent on plasma geometry, magnetic field, plasma current, and ion temperature.
27. This is justified for the data considered here provided $n_e(0) \gtrsim 1.5 \times 10^{20}\,\mathrm{m}^{-3}$.
28. J. M. MANLEY AND H. E. ROWE, *Proc. IRE*, **44**, 904, (1956).
29. C. L. FIORE, F. S. MCDERMOTT, J. D. MOODY, M. PORKOLAB, AND T. D. SHEPARD, in *Applications of Radio-Frequency Power to Plasmas-1987*, edited by S. Bernabei and R. W. Motley, AIP Conference Proceedings No. 159 (American Institute of Physics, New York, 1987), p. 258.
30. B. COPPI, in Abstracts of the 1984 Annual Controlled Fusion Theory Conference, Lawrence Livermore National Laboratory, Livermore, CA, (1984), Paper 3A3.
31. B. COPPI, S. COWLEY, P. DETRAGIACHE, R. KULSRUD, F. PEGORARO, AND W. M. TANG, in Plasma Physics and Controlled Nuclear Fusion Research 1984, Proceedings of the 10th International Conference, London, (IAEA, Vienna, 1984), Vol. 2, p. 93.
32. O. GEHRE, O. GRUBER, H. D. MURMANN, D. E. ROBERTS, F. WAGNER, B. BOMBA, A. EBERHAGEN, H. U. FAHRBACH, G. FUSSMANN, J. GERNHARDT, K. HÜBNER, G. JANESCHITZ, K. LACKNER, E. R. MÜLLER, H. NIEDERMEYER, H. RÖHR, G. STAUDENMAIER, K. H. STEUER, AND O. VOLLMER, *Phys. Rev. Lett.*, **60**, 1502, (1988).

33. T. ANTONSEN, B. COPPI, AND R. ENGLADE, *Nucl. Fusion*, **19**, 641, (1979).
34. G. S. LEE, P. H. DIAMOND, in Abstracts of the 1985 Controlled Fusion Theory Conference, University of Wisconsin, Madison, Madison, WI, (1985), Paper 1S24.
35. R. ENGLADE, B. COPPI, S. MIGLIUOLO, in Abstracts of the 1985 Controlled Fusion Theory Conference, University of Wisconsin, Madison, Madison, WI, (1985), Paper 2Q20.
36. G. S. LEE AND P. H. DIAMOND, *Phys. Fluids*, **29**, 3291, (1986).

FIGURE CAPTIONS

FIG. 1 Location of the hydrogen and deuterium integral and odd–half integral cyclotron harmonics in the poloidal cross–section for (a) $B_0 = 7.6\,\mathrm{T}$ and (b) $B_0 = 9.3\,\mathrm{T}$.

FIG. 2 Hydrogen ion heating rate, $\Delta T_{\mathrm{H}}(0)/P_{\mathrm{rf}}\,(\mathrm{eV/kW})$, as a function of the line–averaged density during rf power injection at $B_0 = 7.6\,\mathrm{T}$. [After Ref. 2]

FIG. 3 Comparison of scattered CO_2 laser power from IBW and low–frequency edge turbulence. (a) Scattered CO_2 laser power from central plasma IBW power as a function of plasma line–averaged density. The dotted line shows the expected value of P_{scat} assuming a large value of $k_{\|}$ ($n_{\|} = 5$). (b) Scattered power from low–frequency edge turbulence as a function of plasma line–averaged density. [After Ref. 3]

FIG. 4 IBW poloidal ray trajectories and radial power deposition as a function of increasing fluctuation amplitude for a plasma line–averaged density of $1.5 \times 10^{20}\,\mathrm{m^{-3}}$ and $B_0 = 7.6\,\mathrm{T}$.

FIG. 5 IBW poloidal ray trajectories and radial power deposition as a function of increasing fluctuation amplitude for a plasma line–averaged density of $2.7 \times 10^{20}\,\mathrm{m^{-3}}$ and $B_0 = 7.6\,\mathrm{T}$.

FIG. 6 The calculated IBW central power deposition. (a) Predicted fraction of IBW power reaching the plasma region $\rho/a \leq 0.5$ as a function of plasma line–averaged density. (b) Measured fluctuation power and corresponding assumed fluctuation amplitude as a function of plasma line–averaged density.

FIG. 7 Ohmic discharge characteristics at $B_0 = 7.6\,\mathrm{T}$. (a) Inferred value of the ion thermal conduction anomaly during Ohmic heating as a function of line–averaged density. $B_0 = 7.6\,\mathrm{T}$. (b) Ohmic Z_{eff} value measured from visible bremsstrahlung as a function of line–averaged density. $B_0 = 7.6\,\mathrm{T}$.

FIG. 8 Individual components of the ion power flow during Ohmic heating at $\rho/a = 0.75$ as a function of line–averaged density. $B_0 = 7.6\,\mathrm{T}$. Individual powers shown are fractions of total integrated Ohmic power.

FIG. 9 The inferred value of the ion thermal conduction anomaly during Ohmic and IBW heating as a function of line–averaged density assuming that (a) 0.3–0.6 P_{rf} flows into the hydrogen and the fluctuation amplitude is between 0 and

0.4 at $\bar{n}_e = 3 \times 10^{20}\,\mathrm{m}^{-3}$ and (b) $0.6\,P_{rf}$ flows into the hydrogen and that the fluctuation amplitude reaches a value of 0.4 at $\bar{n}_e = 3 \times 10^{20}\,\mathrm{m}^{-3}$. The letter labels indicate data points from the same discharge. $B_0 = 7.6\,\mathrm{T}$.

FIG. 10 The inferred value of the ion thermal conduction anomaly during Ohmic and IBW heating as a function of line–averaged density assuming that (a) $0.3\,P_{rf}$ flows into the hydrogen and that the fluctuation amplitude reaches a value of 40% at $\bar{n}_e = 3 \times 10^{20}\,\mathrm{m}^{-3}$ and (b) $0.6\,P_{rf}$ flows into the hydrogen and that the fluctuation amplitude has a value of 0. The letter labels indicate data points from the same discharge. $B_0 = 7.6\,\mathrm{T}$.

FIG. 11 Simulated ion heating rate $\Delta T_i/P_{rf}$ as a function of line–averaged density. In one case, $P_{rf} = 0$ and the ion temperature increase results only from improved particle confinement. In the other case, $0.6\,P_{rf}$ flows into the hydrogen with a profile given by the scattering results (assuming a 40% fluctuation amplitude at $\bar{n}_e = 3 \times 10^{20}\,\mathrm{m}^{-3}$) and the ion temperature increase results from both improved particle confinement and rf power absorption. $B_0 = 7.6\,\mathrm{T}$.

FIG. 12 Ohmic discharge characteristics at $B_0 = 9.3\,\mathrm{T}$. (a) Inferred value of the ion thermal conduction anomaly during Ohmic heating as a function of the line–averaged density. (b) Ohmic Z_{eff} measured by visible bremsstrahlung as a function of the line–averaged density. $B_0 = 9.3\,\mathrm{T}$.

FIG. 13 Individual components of the ion power flow as a function of the line–averaged density at radial locations (a) $\rho/a = 0.5$, (b) $\rho/a = 0.75$. $B_0 = 9.3\,\mathrm{T}$. Individual powers shown are fractions of total integrated Ohmic power.

FIG. 14 The inferred value of the ion thermal conduction anomaly during Ohmic and IBW heating as a function of line–averaged density assuming that (a) 0.3–$0.6\,P_{rf}$ flows into the hydrogen and the fluctuation amplitude is between 0 and 0.4 at $\bar{n}_e = 3 \times 10^{20}\,\mathrm{m}^{-3}$ and (b) $0.6\,P_{rf}$ flows into the hydrogen and that the fluctuation amplitude reaches a value of 0.4 at $\bar{n}_e = 3 \times 10^{20}\,\mathrm{m}^{-3}$. The letter labels indicate data points from the same discharge. $B_0 = 9.3\,\mathrm{T}$.

FIG. 15 The inferred value of the ion thermal conduction anomaly during Ohmic and IBW heating as a function of line–averaged density assuming that (a) $0.3\,P_{rf}$ flows into the hydrogen and that the fluctuation amplitude reaches a value of 40% at $\bar{n}_e = 3 \times 10^{20}\,\mathrm{m}^{-3}$ and (b) $0.6\,P_{rf}$ flows into the hydrogen and that the fluctuation amplitude has a value of 0. The letter labels indicate data points from the same discharge. $B_0 = 9.3\,\mathrm{T}$.

FIG. 16 Simulated ion heating rate $\Delta T_i/P_{rf}$ as a function of line–averaged density assuming an Ohmic–like ion thermal conductivity and that $0.6\,P_{rf}$ flows into the hydrogen with a profile given by the scattering results. The ion temperature increase results from both improved particle confinement and rf power absorption. $B_0 = 9.3\,\mathrm{T}$.

FIG. 17 Experimental global energy confinement time during the Ohmic and Ohmic plus IBW heated portions of the discharge as a function of line–averaged density. (a) $B_0 = 7.6\,\mathrm{T}$. (b) $B_0 = 9.3\,\mathrm{T}$.

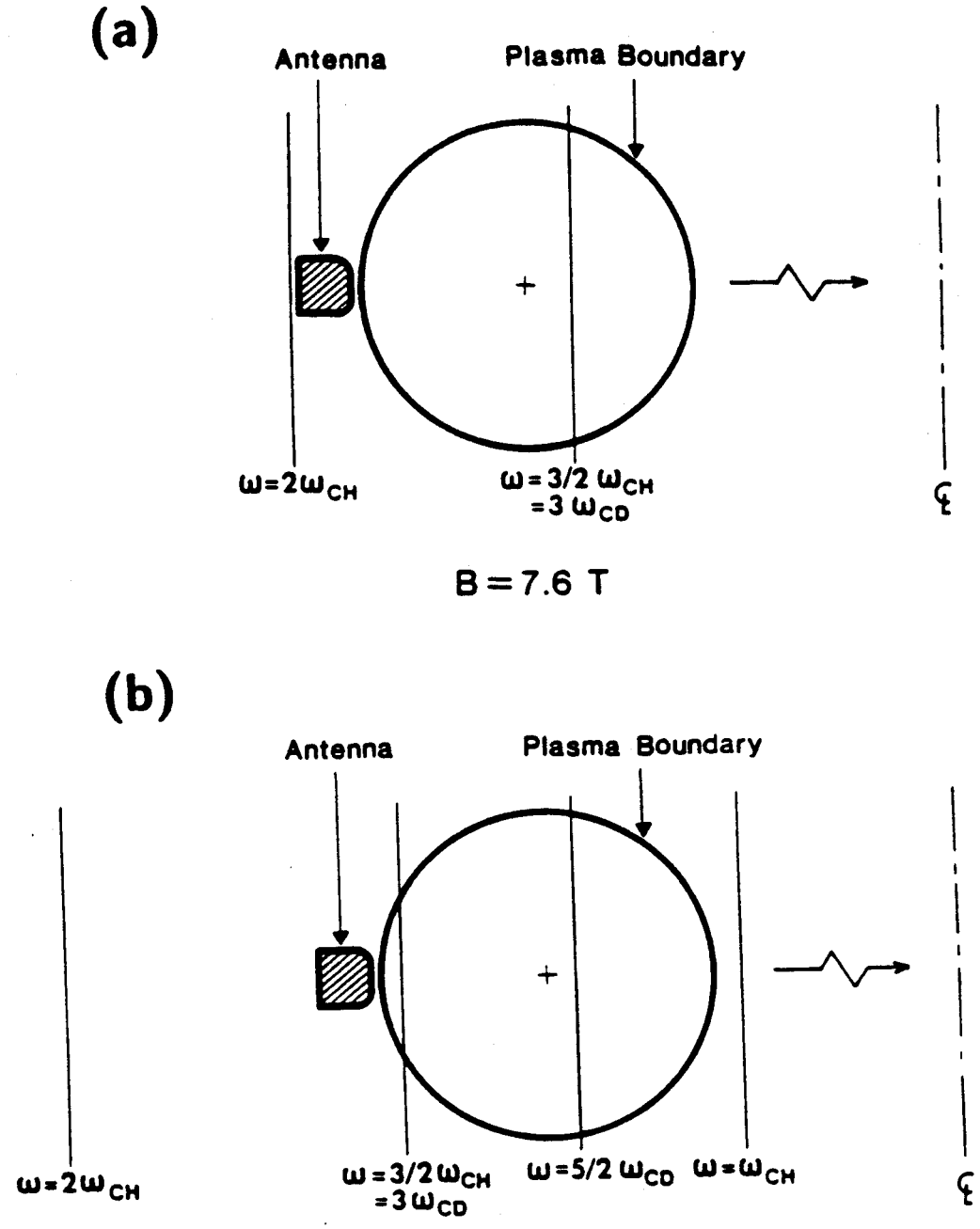
(a)
Antenna
Plasma Boundary
ω=2ω_CH
ω=3/2 ω_CH
=3 ω_CD
B=7.6 T
(b)
Antenna
Plasma Boundary
ω=2ω_CH
ω=3/2ω_CH
=3ω_CD
ω=5/2 ω_CD
ω=ω_CH
B=9.3 T

Figure 1

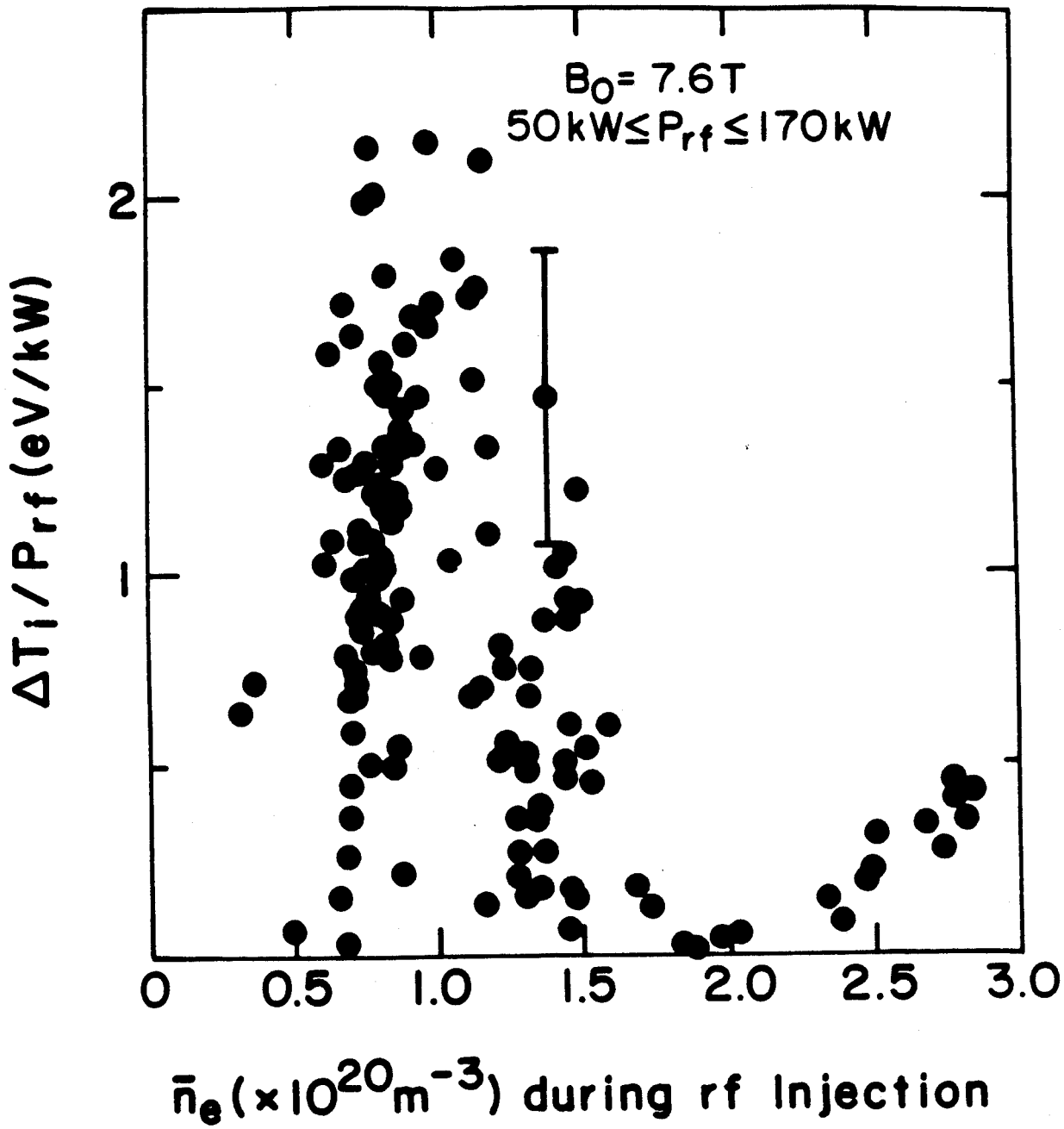
B_0= 7.6T
50kW≤P_{rf}≤170kW
$\Delta T_i / P_{rf}$ (eV/kW)
2
1
0
0.5
1.0
1.5
2.0
2.5
3.0
$\bar{n}_e$ (×$10^{20}$$m^{-3}$) during rf Injection

Figure 2

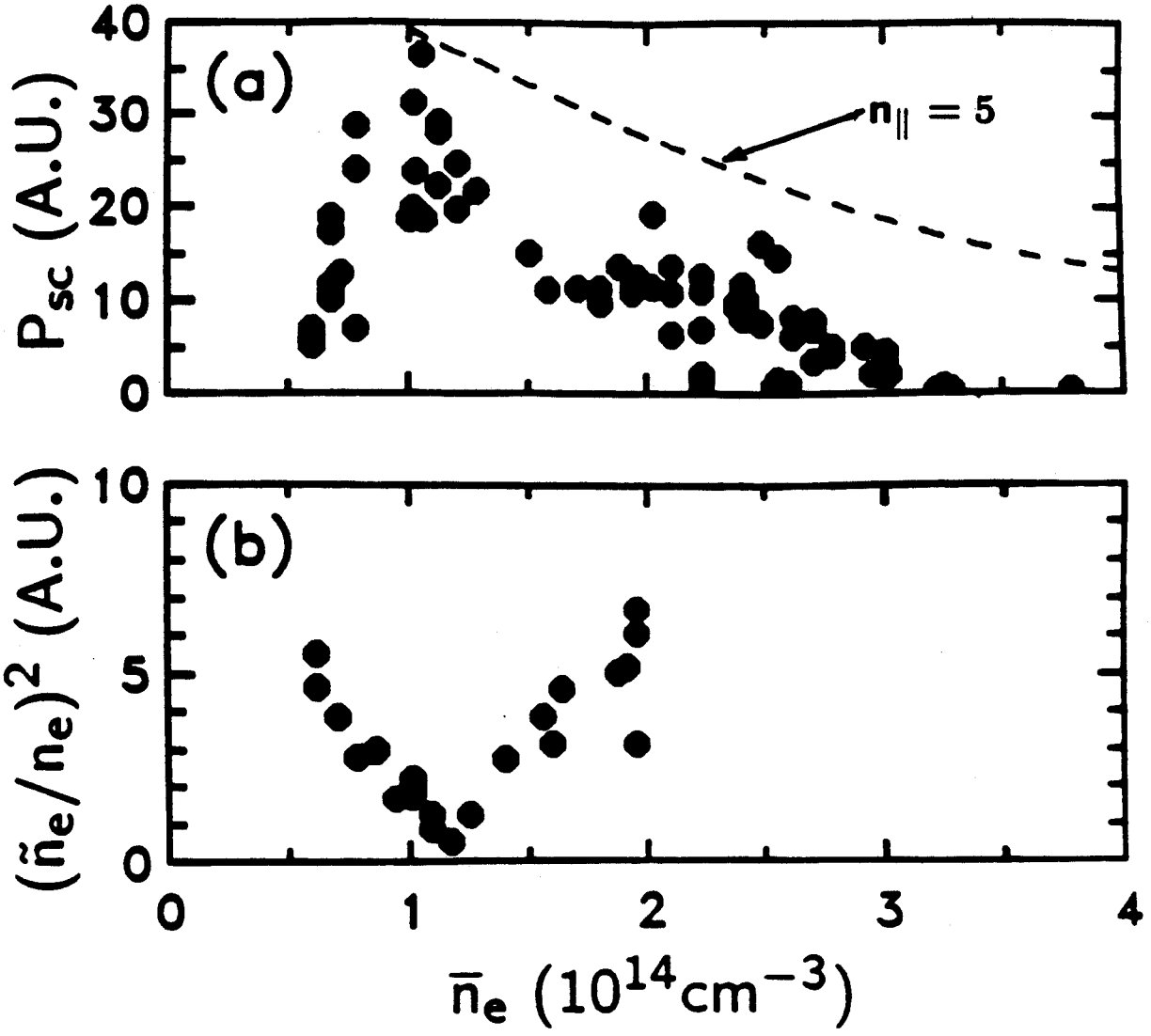
40
30
20
10
0
(a)
P_{sc} (A.U.)
$n_{\parallel} = 5$
10
5
0
(b)
$(\tilde{n}_e/n_e)^2$ (A.U.)
0
1
2
3
4
$\bar{n}_e$ (10^{14}cm^{-3})

Figure 3

$$\bar{n}_e = 1.5 \times 10^{20}\,\mathrm{m}^{-3}$$

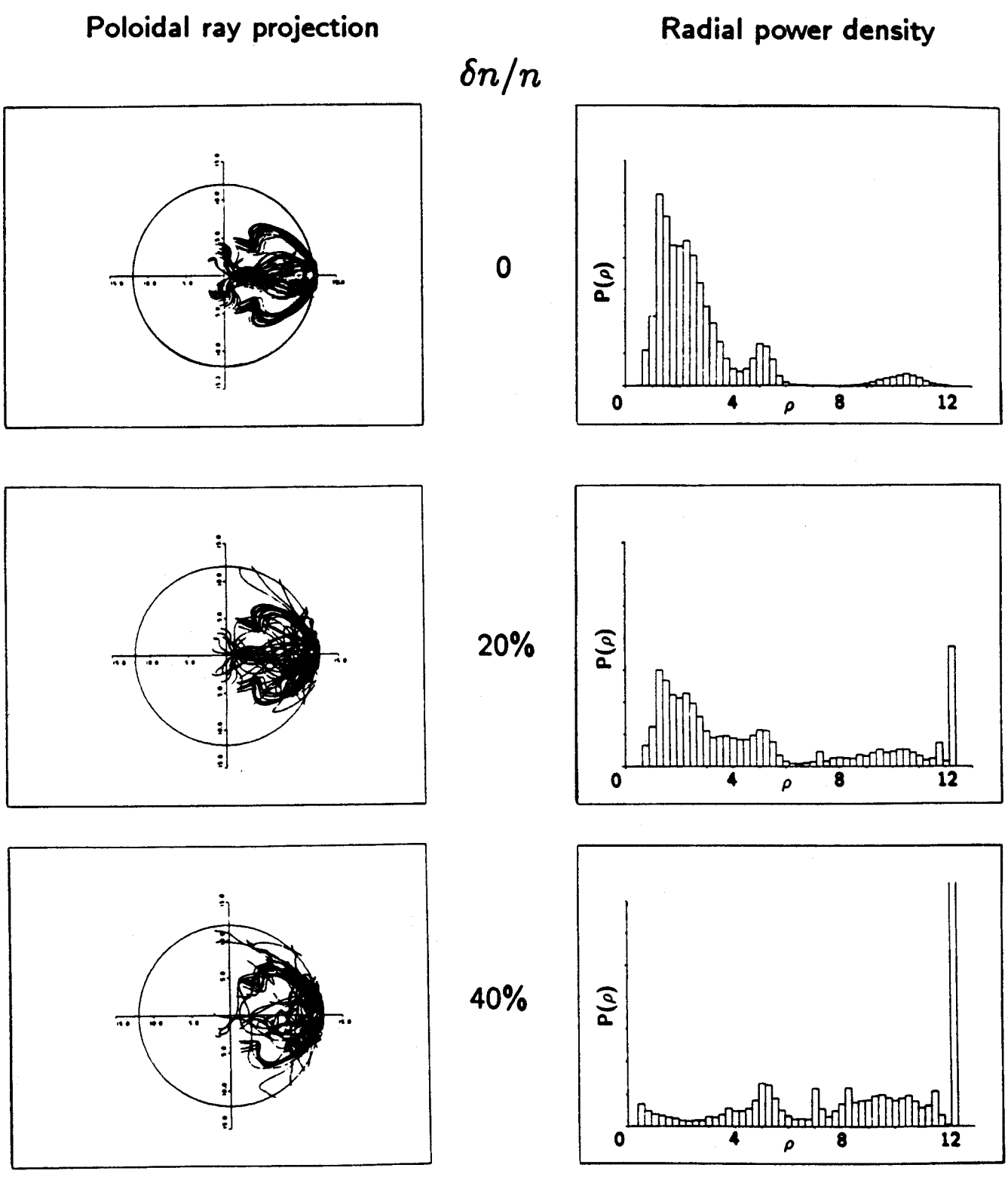

Figure 4

$$\bar{n}_e = 2.7 \times 10^{20}\,\mathrm{m}^{-3}$$

Poloidal ray projection

Radial power density

$\delta n/n$

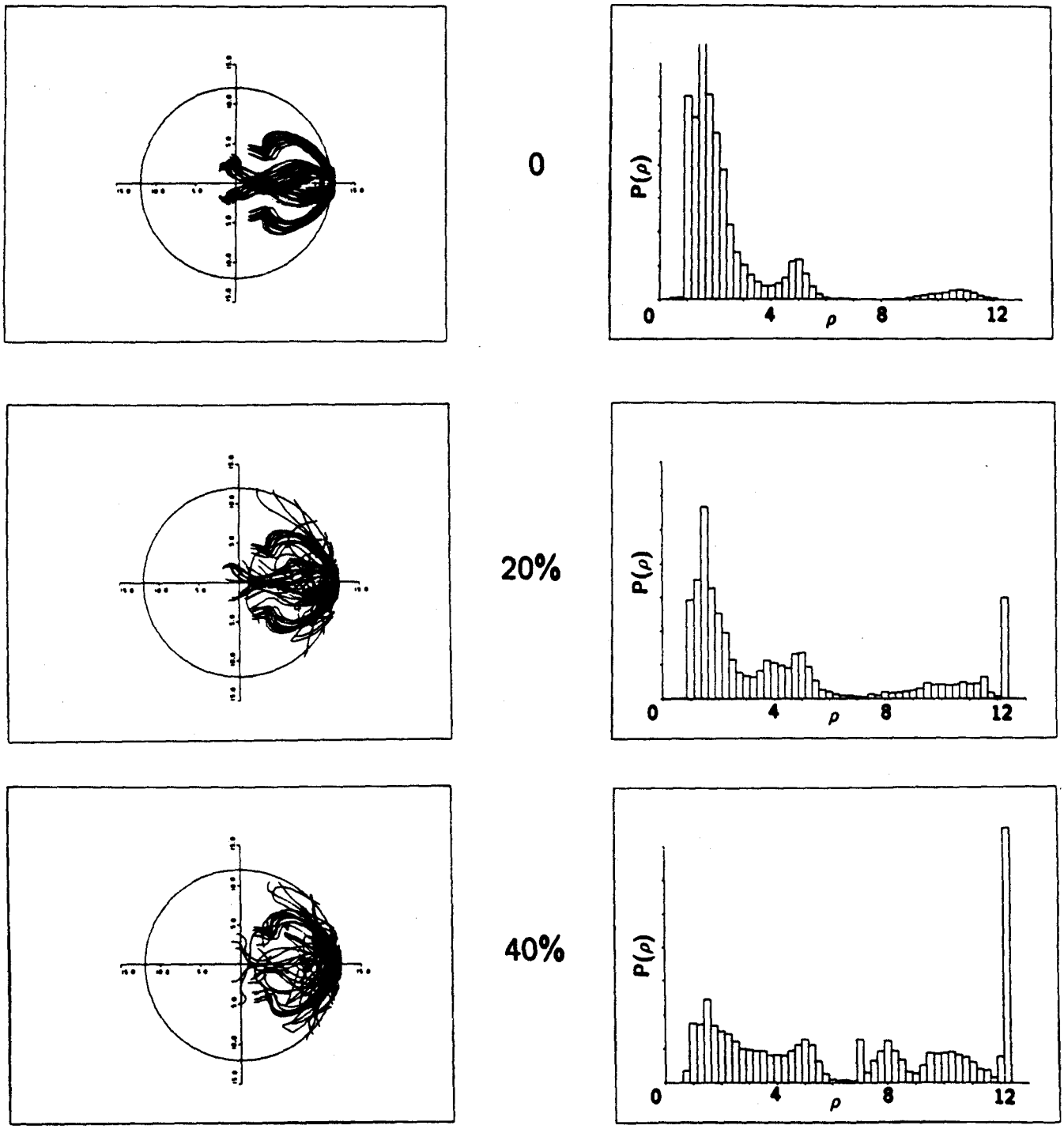

Figure 5

Fraction of Power Deposited in Plasma Center $\rho/a \leq 0.5$

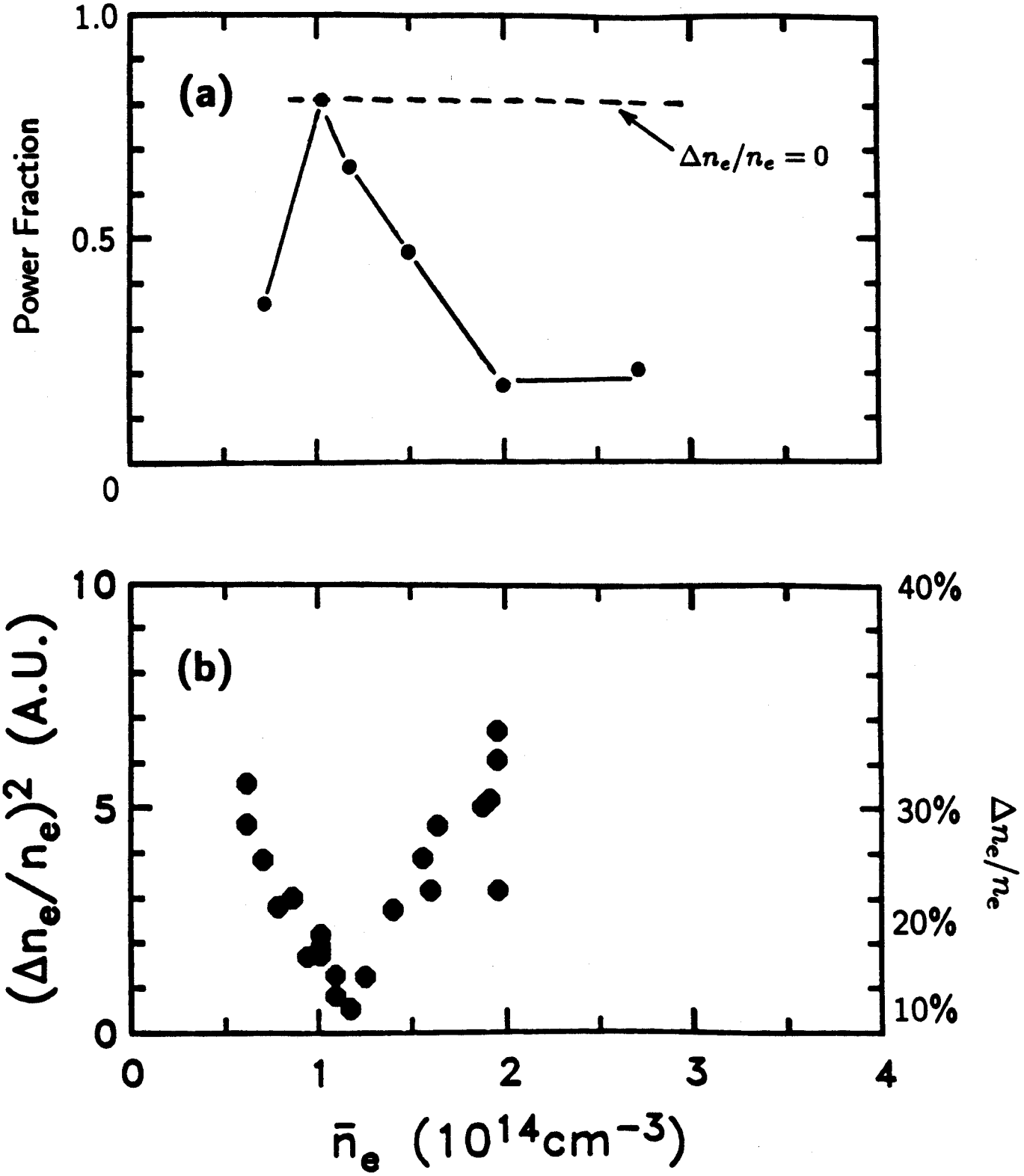

Figure 6

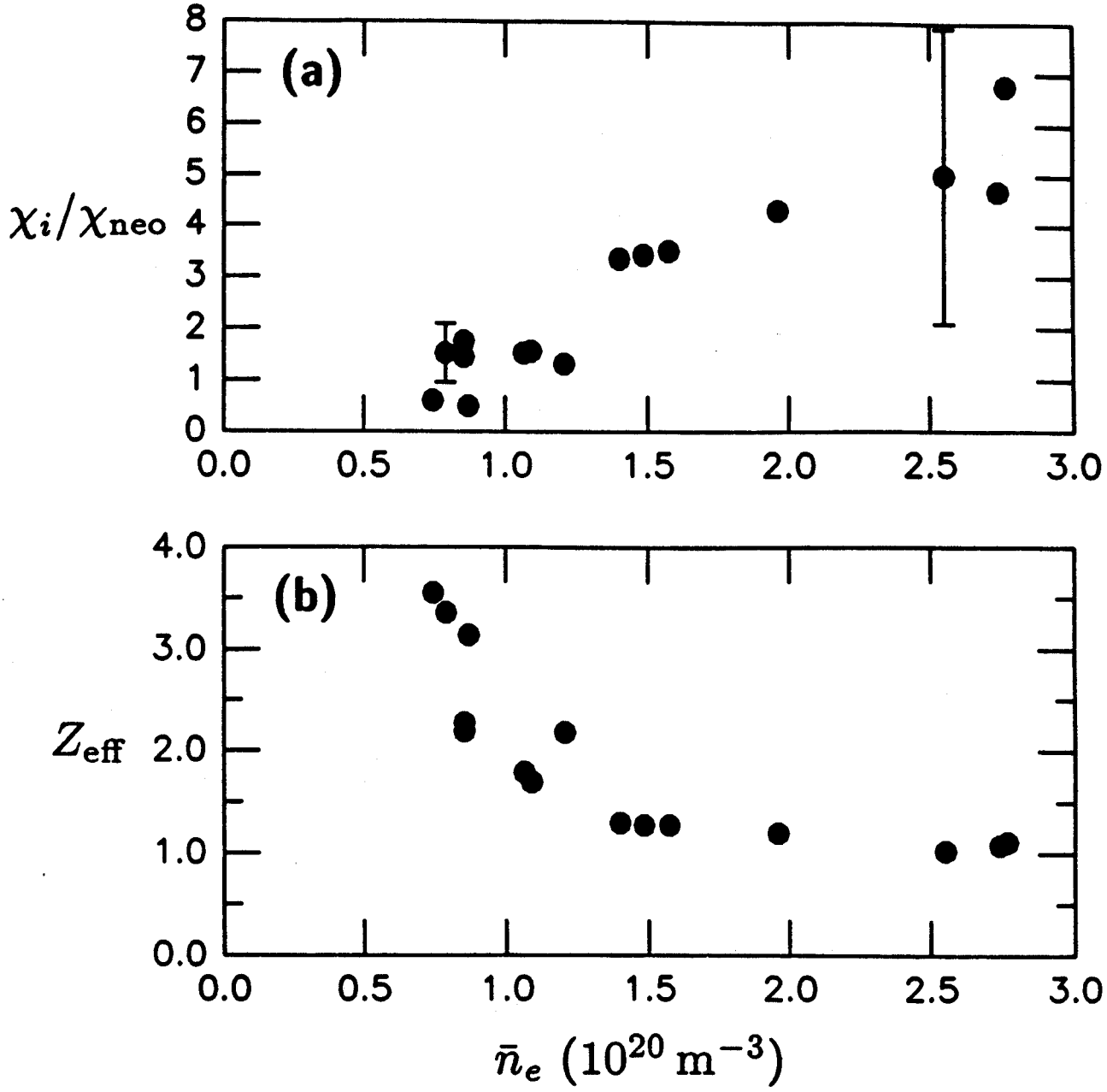
(a)
χ_i/χ_{neo}
0
1
2
3
4
5
6
7
8
0.0
0.5
1.0
1.5
2.0
2.5
3.0
(b)
Z_{eff}
0.0
1.0
2.0
3.0
4.0
$\bar{n}_e$ (10^{20} m^{-3})

Figure 7

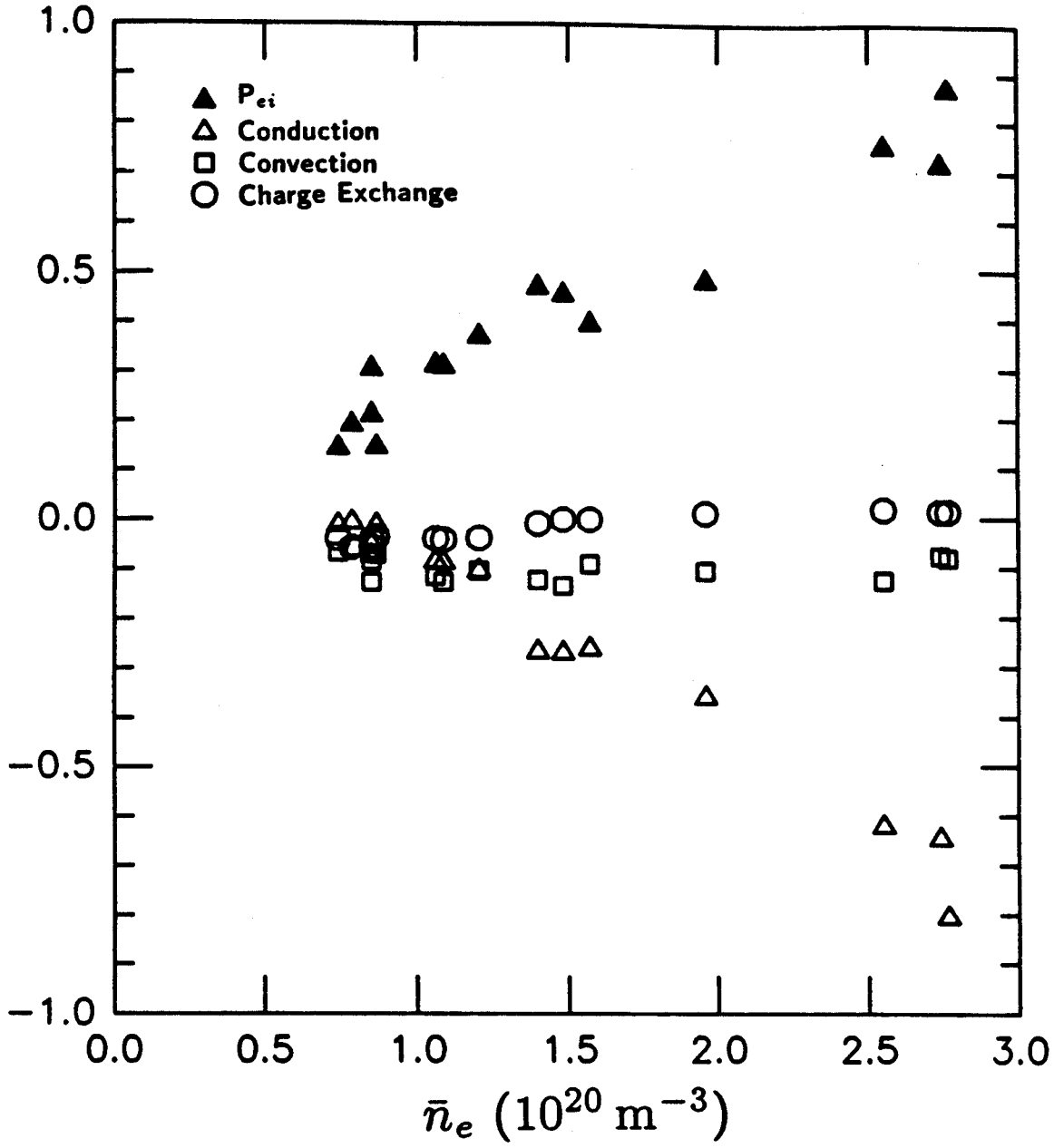
1.0
0.5
0.0
−0.5
−1.0
0.0
0.5
1.0
1.5
2.0
2.5
3.0
P_{ei}
Conduction
Convection
Charge Exchange
$\bar{n}_e\ (10^{20}\,\mathrm{m}^{-3})$

Figure 8

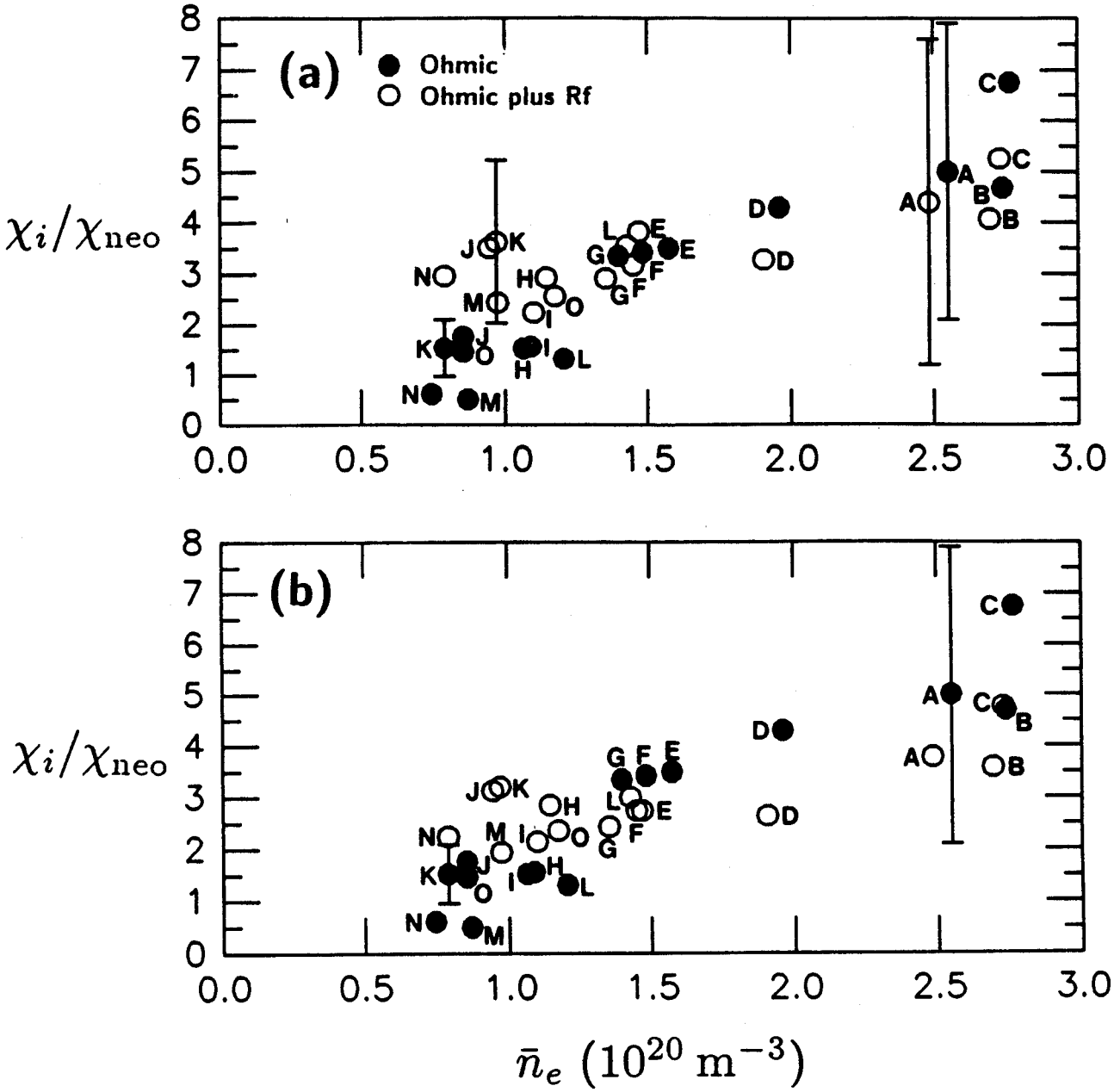

Figure 9

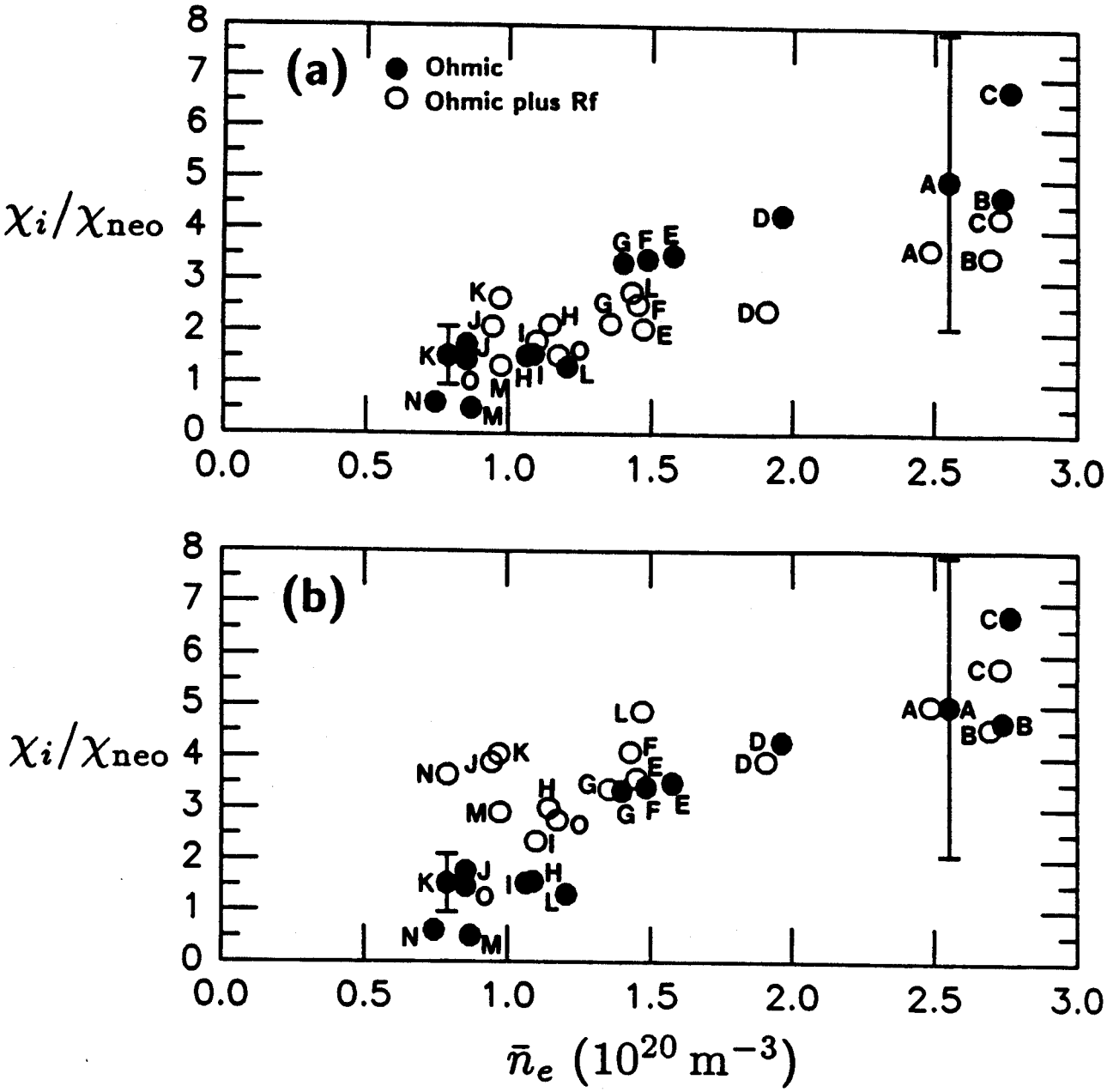
(a)
Ohmic
Ohmic plus Rf
(b)
χ_i/χ_{neo}
$\bar{n}_e$ $(10^{20}\,m^{-3})$
0.0
0.5
1.0
1.5
2.0
2.5
3.0
0
1
2
3
4
5
6
7
8

Figure 10

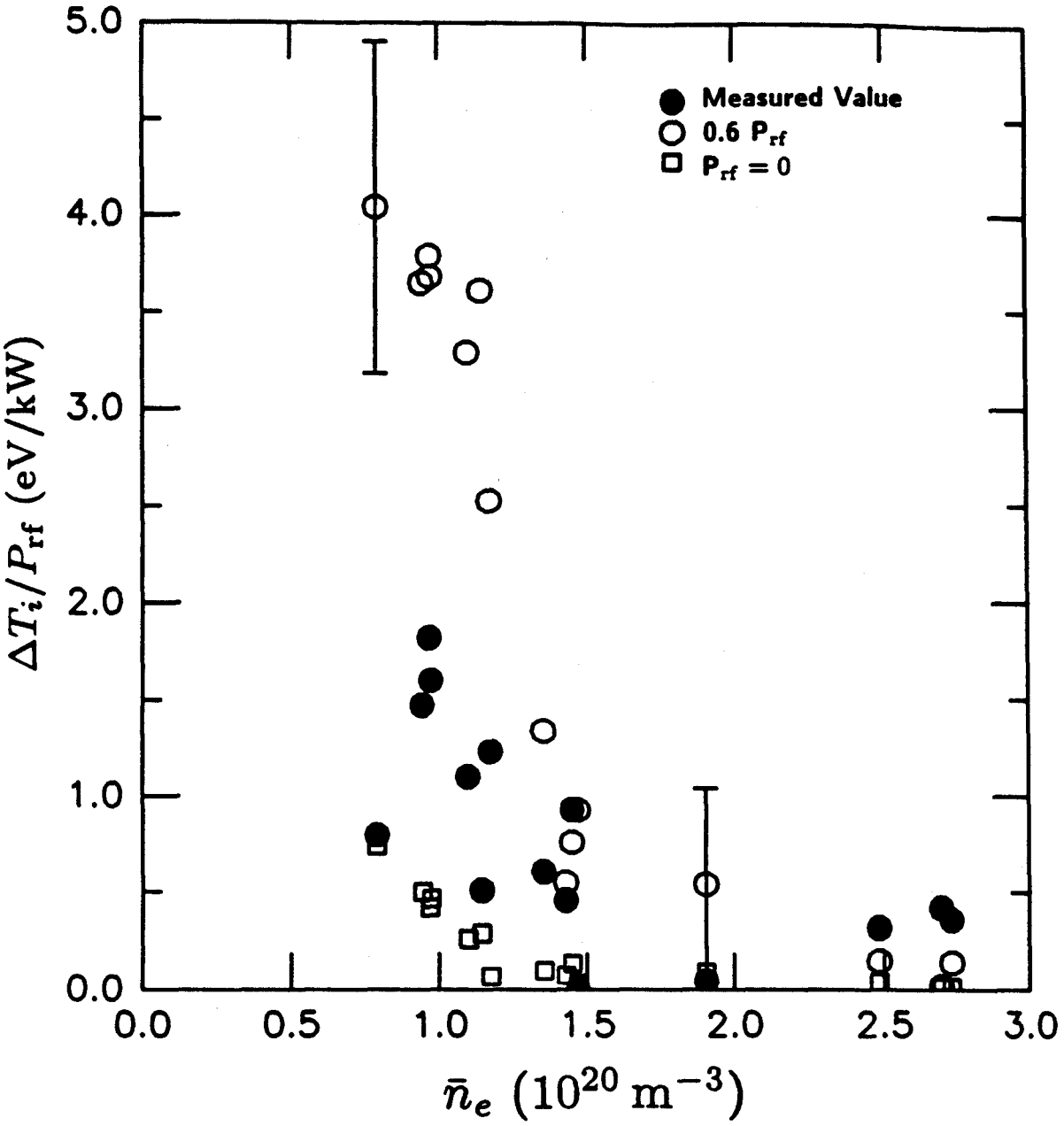
Measured Value
0.6 P_{rf}
$P_{rf} = 0$
$\Delta T_i/P_{rf}$ (eV/kW)
$\bar{n}_e$ (10^{20} m^{-3})
0.0
1.0
2.0
3.0
4.0
5.0
0.0
0.5
1.0
1.5
2.0
2.5
3.0

Figure 11

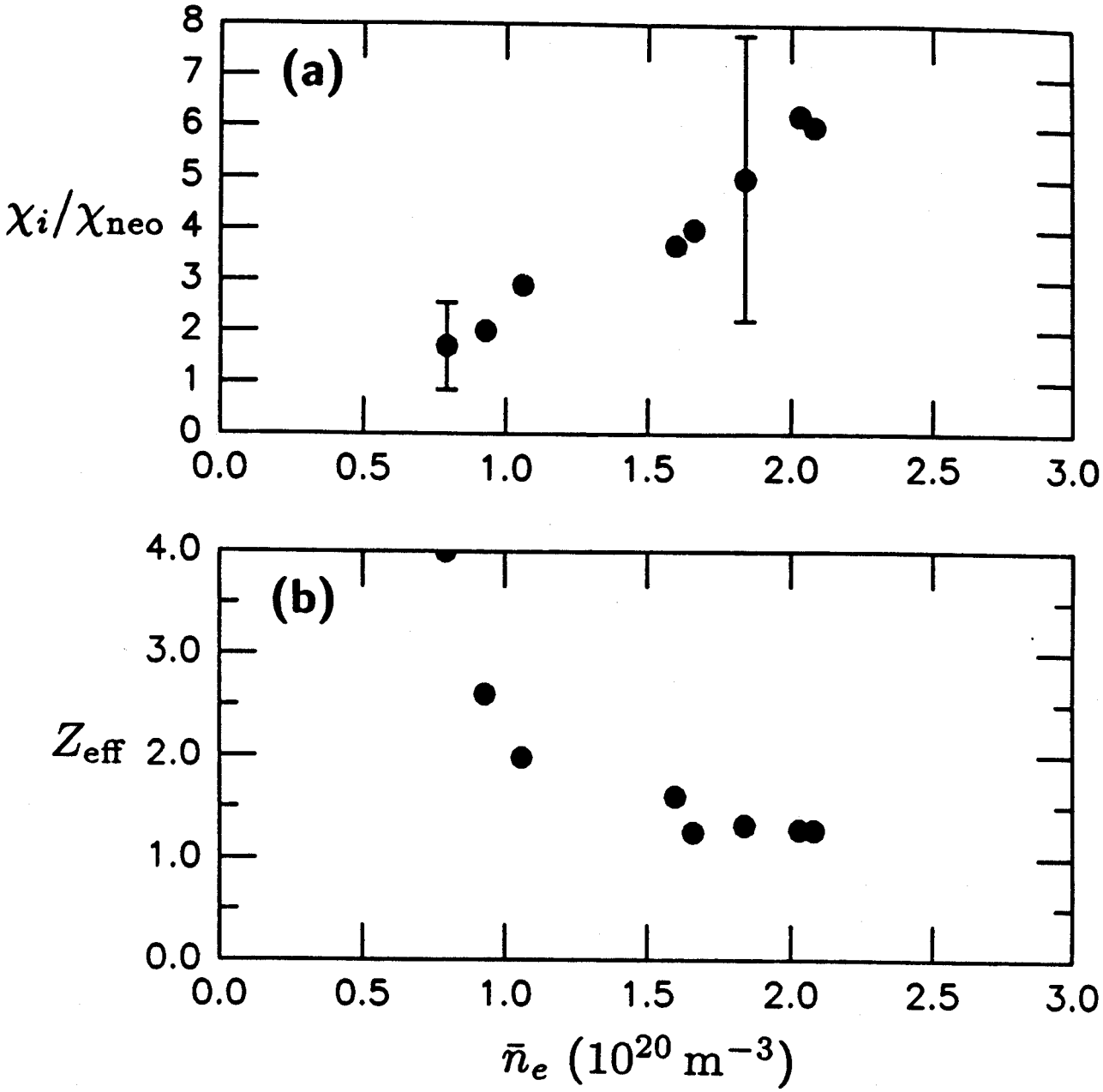
(a)
χ_i/χ_{neo}
8
7
6
5
4
3
2
1
0
0.0
0.5
1.0
1.5
2.0
2.5
3.0
(b)
Z_{eff}
4.0
3.0
2.0
1.0
0.0
$\bar{n}_e$ $(10^{20}\,m^{-3})$

Figure 12

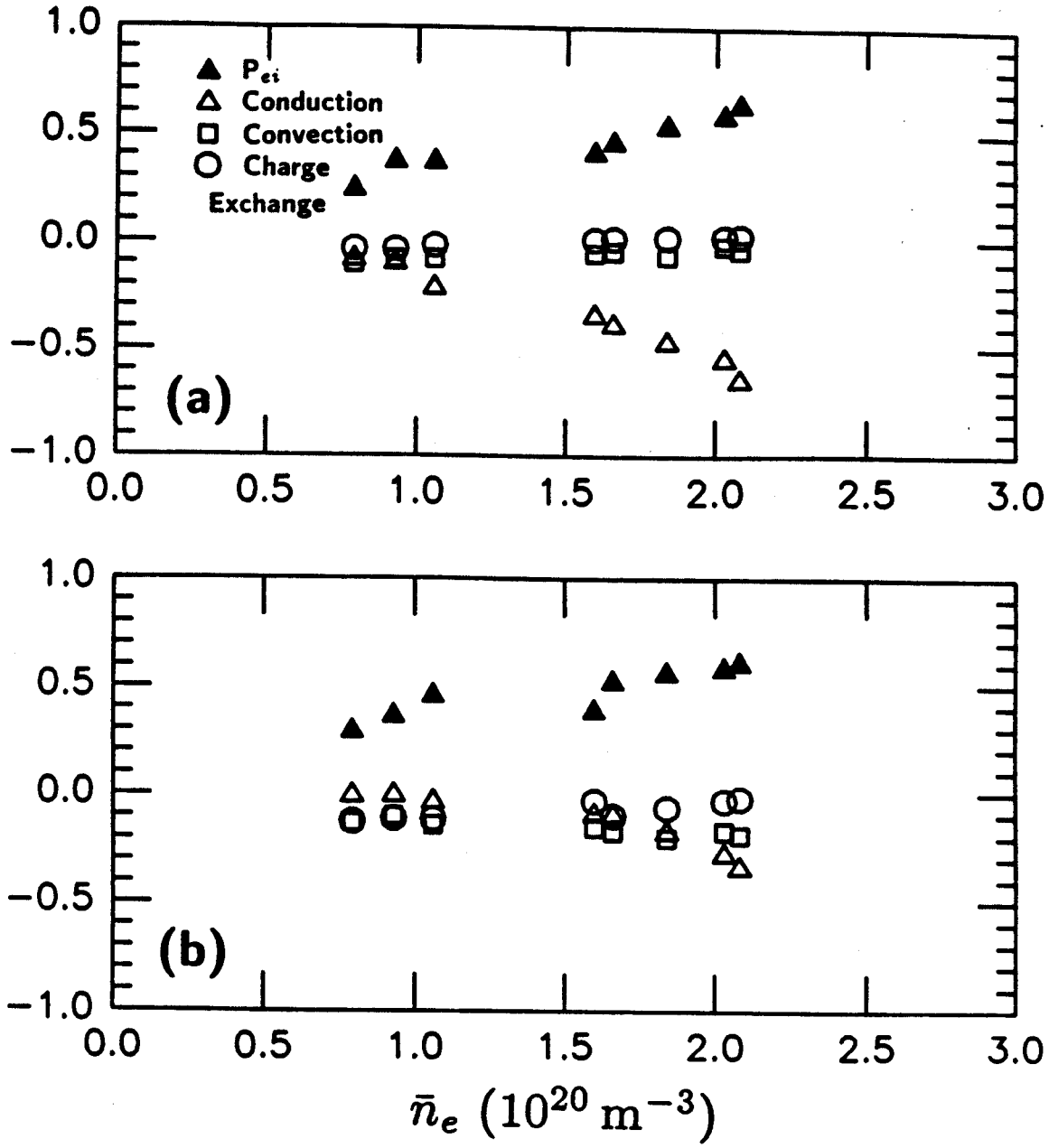
1.0
0.5
0.0
−0.5
−1.0
P_{ei}
Conduction
Convection
Charge Exchange
(a)
(b)
0.0
0.5
1.0
1.5
2.0
2.5
3.0
$\bar{n}_e$ $(10^{20}\,\mathrm{m}^{-3})$

Figure 13

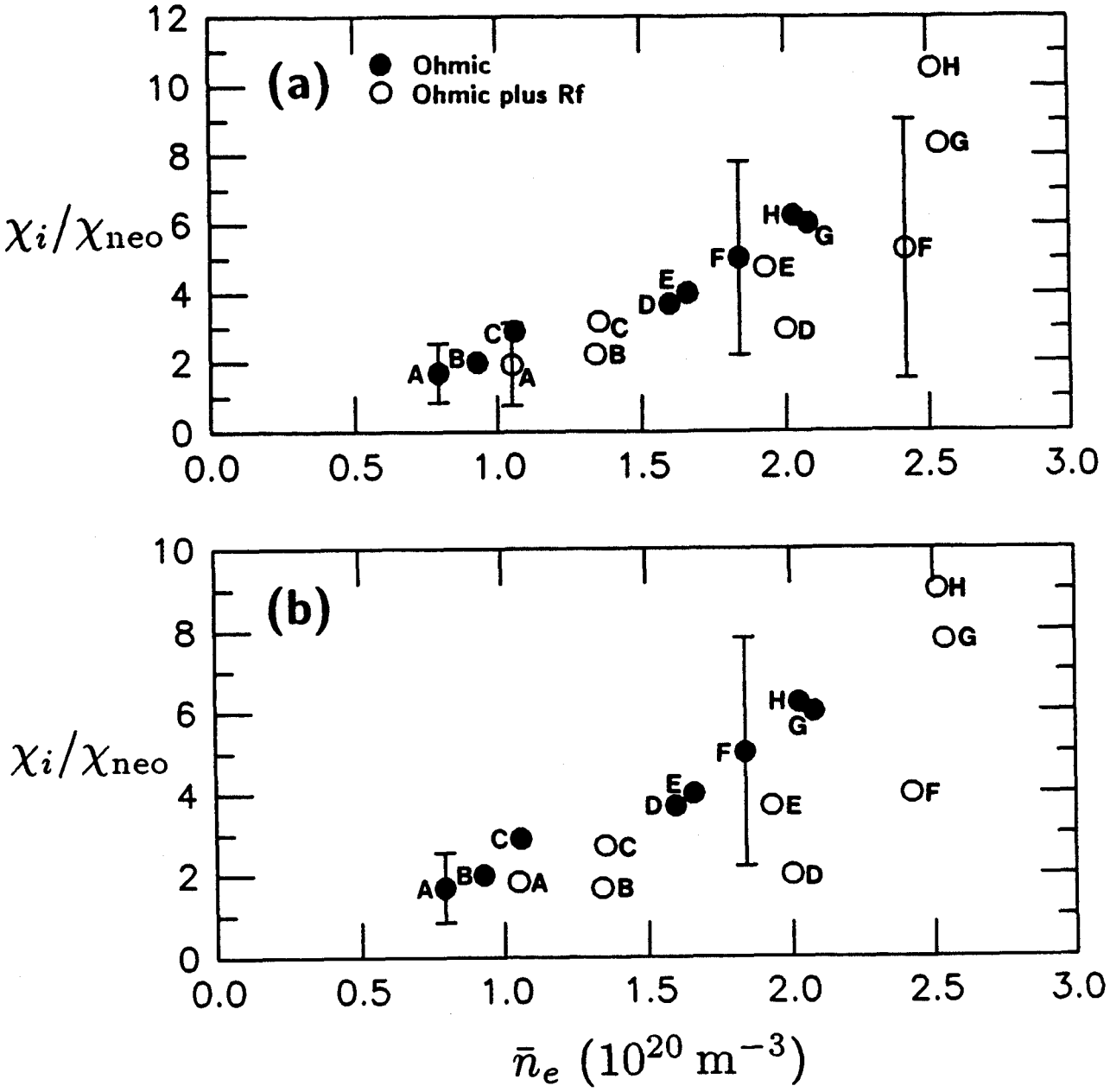
(a)
Ohmic
Ohmic plus Rf
χ_i/χ_{neo}
12
10
8
6
4
2
0
0.0
0.5
1.0
1.5
2.0
2.5
3.0
A
B
C
OA
OB
OC
D
E
F
OD
OE
H
G
OF
OG
OH
(b)
χ_i/χ_{neo}
10
8
6
4
2
0
0.0
0.5
1.0
1.5
2.0
2.5
3.0
$\bar{n}_e$ $(10^{20}\ \mathrm{m}^{-3})$

Figure 14

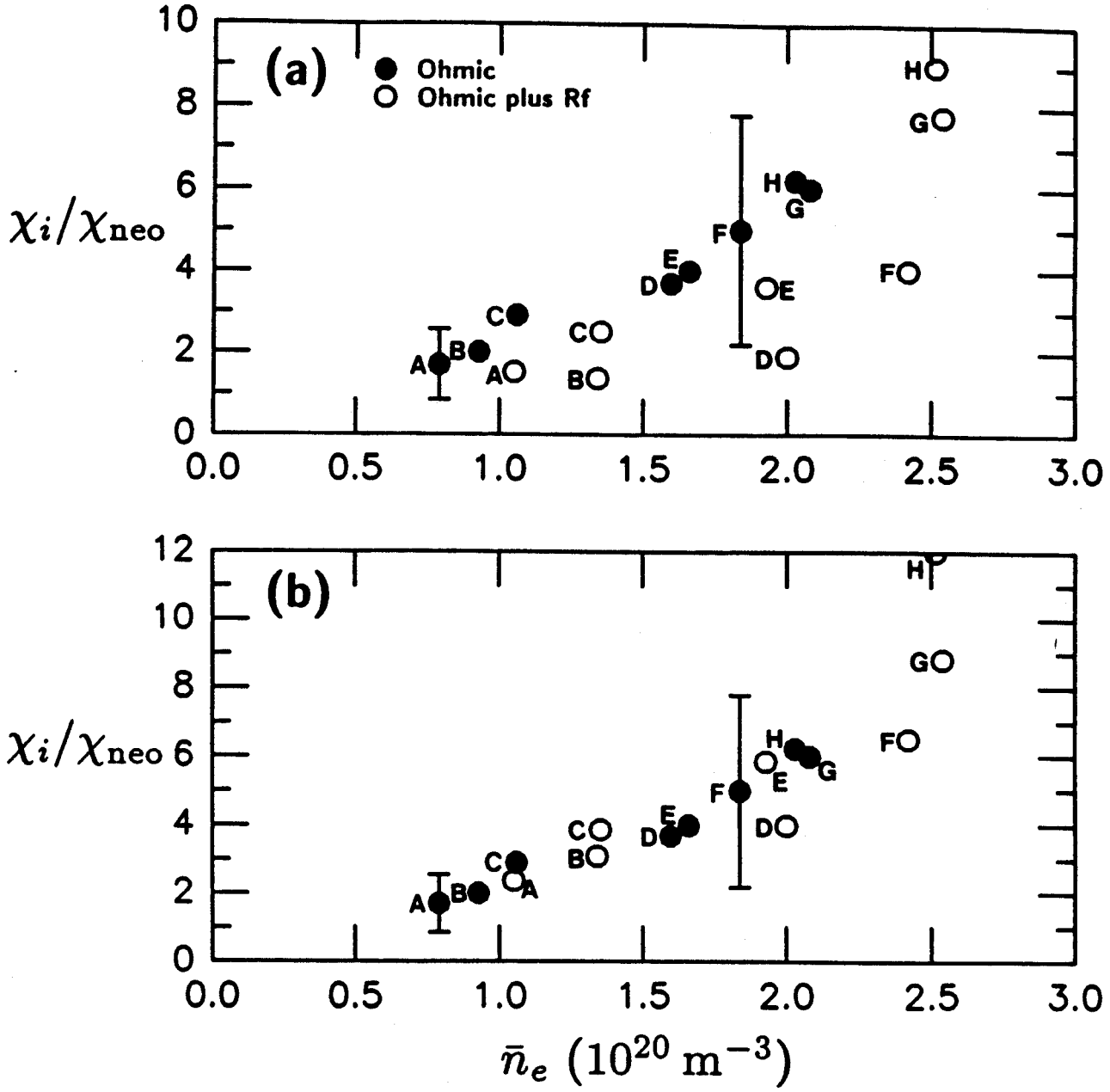

Figure 15

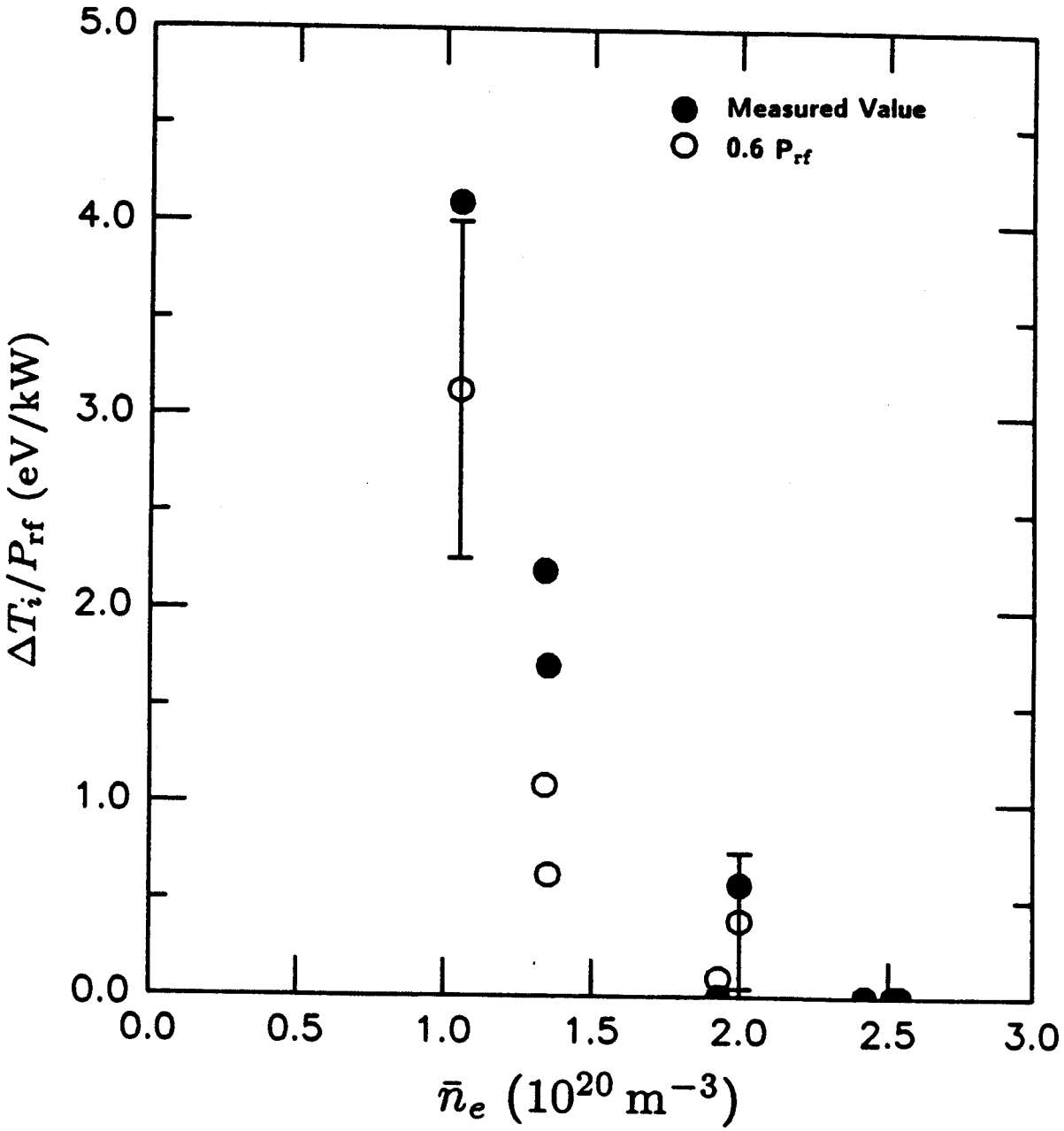
Measured Value
0.6 P_{rf}
$\Delta T_i/P_{rf}$ (eV/kW)
$\bar{n}_e$ (10^{20} m^{-3})
5.0
4.0
3.0
2.0
1.0
0.0
0.0
0.5
1.0
1.5
2.0
2.5
3.0

Figure 16

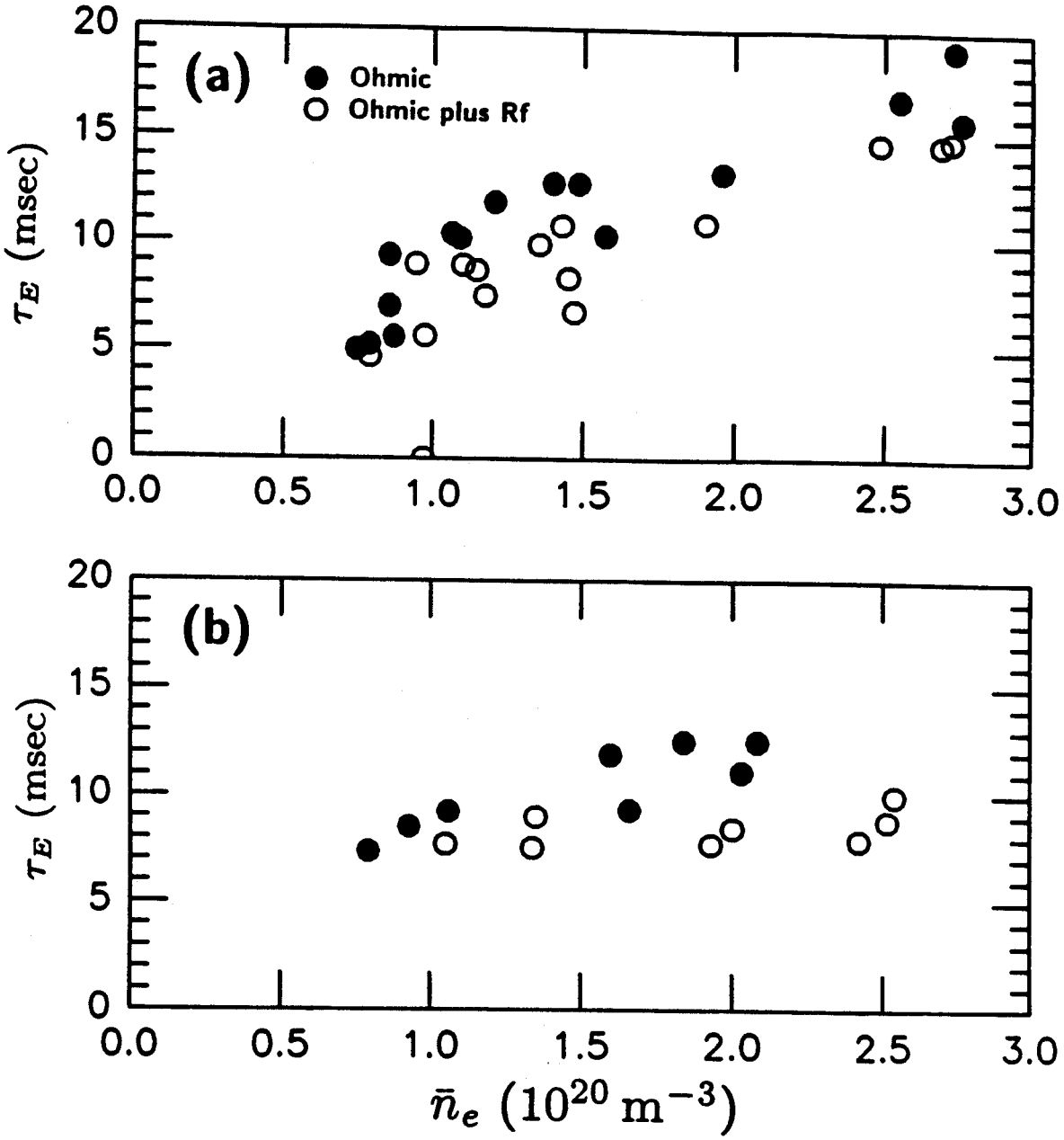
(a)
Ohmic
Ohmic plus Rf
τ_E (msec)
20
15
10
5
0
0.0
0.5
1.0
1.5
2.0
2.5
3.0
(b)
τ_E (msec)
$\bar{n}_e$ (10^{20} m^{-3})

Figure 17